



Università degli Studi di Trieste

DIPARTIMENTO DI FISICA
Corso di Laurea Magistrale in Fisica
Curriculum in Microfisica e Fisica della materia

**Ricostruzione di stati quantistici mediante misura omodina
impulsata applicata alla spettroscopia ultraveloce fuori
equilibrio**

Pulsed homodyne detection for quantum state reconstruction
applied to ultrafast non-equilibrium spectroscopy

Candidato:
Francesco Randi
Matricola SM2300085

Relatore:
Dott. Daniele Fausti
Correlatore:
Prof. Fulvio Parmigiani

Contents

Contents	i
1 Introduction	1
2 Descriptions of the quantum state of a system	5
2.1 Pure states	5
2.2 General quantum states - mixed states	6
3 The quantum harmonic oscillator	9
3.1 Brief review of basic formalism of the harmonic oscillator . . .	10
3.2 The vacuum and coherent states	12
3.3 Squeezed states	16
3.4 Thermal states	19
4 Lowest order light-matter interactions	21
4.1 Modes of the electromagnetic field	21
4.2 Light-matter interaction and the generation of quantum phonon states	23
5 Quantum state reconstruction - Tomography	31
5.1 Balanced homodyne detection	33
6 The experimental set-up	39
6.1 Balanced homodyne detector for pump-probe measurements . .	41
6.2 Noise pump-probe measurements	46
6.3 White light pump-probe measurements	48
6.4 Transient phase-shift measurements	49
7 Bismuth	53
7.1 Jones - Peierls distortion	53

7.2	Unit cell and active phonons	57
7.3	“Coherent phonons”	59
8	Results	63
8.1	Noise in “monochromatic” pump-probe measurements	64
8.2	White light-probe measurements	71
8.3	Transient phase-shift	76
9	Discussion	79
9.1	Possible squeezing of the lattice vibrations	79
10	Conclusions and perspectives	85
A	Time evolution of a coherent state	87
B	Quorum for a two-level system	89
C	D_{3d} point group	91
D	Transient phase-shift and Kramers-Kronig relations	93
E	Acquisition software	95
	Riassunto	97
	Bibliography	103
	Ringraziamenti	107

Chapter 1

Introduction

The kinematics of coherent phenomena in condensed matter is usually described classically. Coherent vibrations of atomic lattices are an example. While the interactions of the vibrational modes with the other degrees of freedom are described as quantum-mechanical processes, the state of the modes, modelled with harmonic oscillators, is usually described with classical parameters, such as amplitude and phase. Little attention has been given to the state's statistical properties, which emerge intrinsically when the system itself is described as a quantum-mechanical object. However, this sort of properties may set stronger constraints on the underlying dynamics and a deeper insight on the quantum state of a system throughout its evolution can be a key step in revealing the Hamiltonians that describe its interactions with the surroundings.

In this thesis, we will study out of equilibrium vibrational states in atomic lattices, which will serve as a benchmark for other kinds of systems. In particular, the background phenomenon that lies at the core of this work is the well known coherent vibrational response observed in pump-probe measurements on Bismuth. In a pump-probe experiment the sample is excited with an intense ultrashort laser pulse (the pump) and its transient optical response is measured using a second ultrashort pulse (the probe). The reflectivity response of Bismuth to the excitation is modulated at the frequency of one of its optical vibrational modes. This means that the pump pulse has excited that mode into a “coherent” state. However, a coherent oscillation of the coordinate of a harmonic oscillator is characteristic of many different quantum states.

To deal with this variety of states, the well established framework of quantum optics can be a very powerful tool, since the modes of the quantized

electromagnetic field are described as harmonic oscillators too. In the past twenty years, a technique has been developed and refined that allows the estimation of the quantum state of the modes of radiation. The process, which allows to reconstruct the density matrix of the state under study, is called quantum tomography. The standard tomographic technique is balanced homodyne detection and it is routinely used in quantum optics laboratories to characterize the final state of a mode of radiation after its interactions with the devices placed on its optical path.

Given these tools, the most natural question is whether information about the state of systems within matter can be mapped into the state of the probe pulses during their interaction (i.e. the reflection). This information could be then retrieved via the tomography of the optical state of the probe pulses. In this thesis we present an experimental set-up we have built in this direction, which is a combination of the standard pump-probe set-up and of a balanced homodyne detector.

The key feature of a balanced homodyne detector is that it allows to observe the distribution of the measurements of the electric field as a function of the phase of the electromagnetic wave. As already mentioned, in some condition pump-probe measurements are phase-resolved for lattice vibrations. When lattice vibrations are mapped in the reflectivity of the sample, the temporal resolution of pump-probe measurements allows to observe the oscillation as it happens. Statistical information about the phononic state can, therefore, be extracted studying the statistics (i.e. the noise) of the measurement of the transient reflectivity of the sample in pump-probe experiments. However, the full reconstruction of the vibrational state is not possible with such a technique, since it cannot be fully tomographic. This is due to the fact that the system evolves while its properties oscillate and there is no stationary state to be studied. Moreover, other factors, such as the interactions with the electrons, which are the ones that mediate the measurement of the atomic displacements, must be considered. Nonetheless, a detailed analysis of noise pump-probe experiments still gives access to partial information about the underlying vibrational state. We present the experimental set-up built to this purpose and report the measured data, which could be a signature of the presence of non-classical states of the harmonic oscillator.

In order to clarify some aspects of the role of the electrons in the mediation of the measurement process we have also performed more conventional pump-probe measurements with broadband white-probes, which give us a clearer picture of the underlying electronic dynamics. Furthermore, the

balanced homodyne detector can be used for another spectroscopic technique. As we will describe, the detector is based on an interferometer. The latter can be employed, in combination with pump-probe measurements, to detect the transient phase-shifts in the out of equilibrium field-reflectivity. Here only preliminary results obtained with this set-up will be presented.

Chapter 2

Descriptions of the quantum state of a system

This introductory chapter is mainly inspired by a review paper by Ugo Fano (see [1]) and serves the purpose to introduce conceptual tools, such as the density matrix and the Wigner function, which are used to describe the quantum state of a system. Some sentences, being so clearly expressed by Fano, are reported verbatim.

2.1 Pure states

There are states, in quantum mechanics, which are characterized by the fact that the information about the system under consideration is known in the most deterministic way permitted by quantum mechanics itself [1]. Such states are called *pure* states and the information about them is encoded in a normalized vector $|\Psi\rangle$. The latter belongs to a Hilbert space \mathcal{H} , which contains all the possible states of that system. These vectors can be conveniently represented in one of the bases for \mathcal{H} and can therefore be expressed as a wavefunction $\Psi(t, \vec{r})$ or as a full set of quantum numbers such, for example, (n, l, j, m) for a non-relativistic electron in a hydrogenic potential. For pure states an experiment exists, at least in principle, whose outcome is unique and predictable with certainty when performed on a system prepared in that state and a measurement of this kind is called “complete”, for it provides the maximum amount possible of information about that variable of the system. In the formalism of vector states, the expectation value of an observable, identified by an Hermitian operator \hat{O} acting on the Hilbert space \mathcal{H} of the state,

is given by

$$\langle \hat{O} \rangle_{\Psi} = \langle \Psi | \hat{O} | \Psi \rangle.$$

An alternative writing for this expression, which will be useful in the discussion of mixed states, is

$$\langle \Psi | \hat{O} | \Psi \rangle = \text{Tr}[\hat{O} | \Psi \rangle \langle \Psi |]$$

and it suggests that a state can also be identified by the projector $|\Psi\rangle\langle\Psi|$. It is important to note that it can happen that a pure state is most conveniently described as a linear superposition of eigenstates of a particular observable \hat{O}_1 . Nonetheless, it is possible, at least in principle, to design an experiment which probes another observable \hat{O}_2 of the system, whose outcome is predictable with certainty.

2.2 General quantum states - mixed states

However, *systems also occur for which no complete experiment gives a unique outcome predictable with certainty. The state of the system is nevertheless fully identified by any data adequate to predict the (statistical) result of all conceivable observations of the system. Whether or not the predicted dispersion of these statistical results attains its theoretical minimum is irrelevant to the concept of state. Indeed "state" means whatever information is required about a specific system, in addition to physical laws, in order to predict its behavior in future experiments.* This information can be encoded in the density matrix $\hat{\rho}$, an operator on the Hilbert space \mathcal{H} . As mentioned before, pure states can be identified by the projectors $|\Psi\rangle\langle\Psi|$. The density matrix is a generalization of this point of view and it can be written as the weighted sum of projectors

$$\hat{\rho} = \sum_i \lambda_i |\Psi_i\rangle\langle\Psi_i|. \tag{2.1}$$

In this expression, apart from the vectors $|\Psi_i\rangle$ having to be normalized, the coefficients λ_i must satisfy the following two conditions:

$$\sum_i \lambda_i = 1, \quad \lambda_i \geq 0.$$

In the case in which just one of the coefficients λ_i is different from 0, the density matrix $\hat{\rho}$ identifies a pure state, while when there are at least two of them different from 0, the state is a general one and it is said to be a *mixed* state. Note that, being 2.1 just one of the possible representations of $\hat{\rho}$, the choice of the set of $|\Psi_i\rangle$ is not unique.

The expectation value of an observable \hat{O} on the state identified by $\hat{\rho}$ is given by

$$\langle \hat{O} \rangle_{\hat{\rho}} = \text{Tr}(\hat{O}\hat{\rho}). \quad (2.2)$$

This last equation offers a more general definition of the density matrix, by making no reference to any particular set of pure states, as equation 2.1 instead does.

The task of experimentally determining the state of a quantum system consists in gathering all the information needed to perform the predictions about the future behaviour of the system (like 2.2) and the process is called *quantum tomography* of the state, which will be discussed in more detail in Chapter 5.

The Wigner function A useful object, which allows a direct visualization of the state of a system, is a particular transform (the Wigner transform or Weyl anti-transform) of the density matrix: the Wigner function, defined as follows

$$W(q, p) = \int_{-\infty}^{+\infty} dy \langle q + y | \hat{\rho} | q - y \rangle e^{-2iyp/\hbar} \quad (2.3)$$

or symmetrically in p . $W(q, p)$ is a function in the phase-space, i.e. a space spanned by two conjugate variables, usually denoted with q and p . It behaves like a quasi-probability distribution for the quantum state. This means, first of all, that its marginal distributions are the probability densities of the state in the two conjugate variables:

$$\begin{aligned} \int_{-\infty}^{+\infty} dp W(q, p) &= |\Psi(q)|^2, \\ \int_{-\infty}^{+\infty} dq W(q, p) &= |\chi(p)|^2. \end{aligned} \quad (2.4)$$

Moreover, expectation values of observables are simple phase-space averages of their Wigner transforms, i.e., by taking the function

$$o(q, p) = \int_{-\infty}^{+\infty} dy \langle q + y | \hat{O} | q - y \rangle e^{-2iyp/\hbar}$$

the expectation value of \hat{O} will be

$$\langle \hat{O} \rangle = \int_{-\infty}^{+\infty} dq dp W(q, p) o(q, p). \quad (2.5)$$

This last expression resembles $\langle \hat{O} \rangle = \text{Tr}(\hat{O}\hat{\rho})$.

For the systems which we will study in this thesis and which are modeled with quantum harmonic oscillators, q and p will be either actual spatial displacement and momentum or the real and imaginary part of the complex electric field (which play the role of position and momentum in the quantization of the modes of the electromagnetic field).

The Wigner phase space approach is very useful in these cases, since the most common states are represented by simple (namely, gaussian) Wigner functions. Moreover some of the interactions of the system with external objects can be viewed as simple transformations (translations and deformations) of these gaussian functions in phase-space.

Chapter 3

The quantum harmonic oscillator

Both the kinds of systems which we deal with in this thesis, i.e. the modes of the electromagnetic field and the vibrational modes in condensed matter lattices, can be described as quantum harmonic oscillators. For the modes of the electromagnetic field, the oscillator *coordinate* \hat{q} and *momentum* \hat{p} are the real and imaginary part of the complex electric field and the mode excitations are called photons. In the second case \hat{q} and \hat{p} are actual spatial normal mode displacement and momentum and the mode excitations are called phonons. Although both photons and phonons are bosons and their abstract description could seem fairly similar, some relevant differences have to be pointed out [2]. As a first point, the dispersion for photons in vacuum (i.e. the energy of a photon as a function of the momentum of the mode which it is created in) is linear. On the other side, phonons can have many different non-linear dispersion relations, usually with several acoustic and optical branches. These complications make it more difficult, in the phonon case, to match both the conservation of momentum and energy in multimode processes. More importantly to our discussion here, phonons and photons display very different interactions. Photons do not interact one with another unless they are within non-linear optical media and in high number (i.e. high intensities). In such a situation, their interaction is mediated by matter. Instead, phonons do always interact one with another because of the anharmonicity of the potentials which atoms lie in. Furthermore, the condensed matter environment offers phonons many other excitations in their energy-range to couple with. The dynamics of these particles is therefore extremely dissipative if compared to the propagation of photons in transparent media. This leads, for example, to very short

lifetimes for coherent vibrational excitations (of the order of the picoseconds), especially for modes in the optical branches. It has also to be considered that, being the energies of phonons very small (tens of millielectronvolts), the vibrational modes are thermally populated even at room temperature. For the electromagnetic modes one usually works with, instead, the photon energies are much higher than the room temperature $k_B T = 25$ meV, and thus, the thermal photon population of the mode is often negligible.

3.1 Brief review of basic formalism of the harmonic oscillator

The first step in the description of a system through a quantum harmonic oscillator is to identify two variables that behave like the conjugate position and momentum of a harmonic oscillator. In the case of the vibrational modes they are the normal mode displacement and linear momentum. For the modes of the electromagnetic field, instead, they are the real and imaginary parts of the complex time-evolving electric field, also known as quadratures. We will spend more words on the quadratures observables and on their generalization in chapter 5, where their major role in the reconstruction of optical states will be made clear.

Once these quantities have been identified, the procedure is a straightforward application of the standard quantization of the harmonic oscillator. We will use, throughout this thesis, the units in which $\hbar = 1$ and we will put the masses and the frequencies of the harmonic oscillators under consideration to 1 (unless otherwise specified). We will do this, not just as a convenience in the formalism, but also as a safe experimental simplification. In this framework, the measurements of the observables of the harmonic oscillator that have to be quantitative are always associated with reference measurements used to define the units. With this convention, the Hamiltonian for the free oscillator is

$$\hat{H}_0 = \left(\hat{a}^\dagger \hat{a} + \frac{1}{2} \right) \quad (3.1)$$

where \hat{a}^\dagger and \hat{a} are the creation and annihilation operators, respectively. The position and momentum observables can be written as

$$\hat{q} = \frac{1}{\sqrt{2}}(\hat{a} + \hat{a}^\dagger) \quad (3.2)$$

and

$$\hat{p} = \frac{1}{i\sqrt{2}}(\hat{a} - \hat{a}^\dagger). \quad (3.3)$$

The operators \hat{q} and \hat{p} are conjugated observables, i.e. their commutator

$$[\hat{q}, \hat{p}] = i$$

and must therefore satisfy the Heisenberg uncertainty relation

$$\sigma^2(\hat{q})\sigma^2(\hat{p}) \geq \frac{1}{4}. \quad (3.4)$$

$\sigma^2(\hat{O})$ is the variance in the distribution of the outcomes of measurements on the observable \hat{O} , and is defined as $\langle \hat{O}^2 \rangle - \langle \hat{O} \rangle^2$.

The most natural states to work with in this formalism are the number states $|n\rangle$, eigenstates of the Hamiltonian H_0 and therefore also of the number operator $\hat{n} = \hat{a}^\dagger \hat{a}$:

$$\hat{n}|n\rangle = \hat{a}^\dagger \hat{a}|n\rangle = n|n\rangle.$$

They can be written as

$$|n\rangle = \frac{(\hat{a}^\dagger)^n}{\sqrt{n!}}|0\rangle$$

and describe states in which the oscillator is populated with exactly n excitations. The ground state of H_0 , $|0\rangle$ is known as *vacuum* state and is the one which obeys the following condition

$$\hat{a}|0\rangle = 0.$$

It has a probability density in the *position* observable which is a gaussian centred on the appropriate equivalent of the equilibrium position. With increasing n , the probability densities of number states tend to the time-averaged position-distribution of a classical oscillator. This means that the most probable positions to find the oscillator in become the furthest from the equilibrium one, where a classical oscillator, having the lowest velocity there, spends most of its time. However, the expectation value of the position $\langle \hat{q} \rangle_{|n\rangle}$ is time-independent and equals 0 whatever excited number state the oscillator is in. To get a time-dependent expectation value of \hat{q} , a superposition of states must be taken. Out of these non-number states of the harmonic oscillator the commonest are *coherent* states, which are the closest analogue to classical coherent oscillations. Many other states, with different statistical properties, can be both theoretically and experimentally prepared, like, for example, *squeezed* ones. As already mentioned, for phononic modes the thermal population can be significant and thermal states, which are mixed ones, have therefore to be considered too. Gaussian states (namely, coherent, squeezed and thermal

ones, which are states described by gaussian Wigner functions) are the most common states experimentally produced. The generation of gaussian states and, more generally, the interaction with external degrees of freedom can often be described in a simple framework involving transformations within the class of gaussian states, as will be discussed in chapter 4.

3.2 The vacuum and coherent states

The vacuum

The number-vacuum state $|0\rangle$ turns out to be formally a coherent state, from the definition 3.6 given in the next paragraphs. It is a benchmark to introduce the concept of noise in the measurements of the observables of the quantum harmonic oscillator. The probability distribution $|\Psi_{|0\rangle}(q)|^2$ is a gaussian function (centred on the "equilibrium position" of the harmonic oscillator, which we take to be 0):

$$|\Psi_{|0\rangle}(q)|^2 = \frac{1}{2\sqrt{\pi}}e^{-q^2}.$$

Therefore, if one had an ensemble of identical oscillators in their ground state ¹, the outcomes of the measurements of all their positions would not all be 0 but would, instead, be distributed around 0 according to $|\Psi_{|0\rangle}(q)|^2$. There would be, in other words, noise in the measurement which is intrinsic to the state. The reason to underline this here will be clear in the next sections, e.g. the one about squeezed states, which are states that display intrinsic noise in a less trivial way.

It can be shown that the probability distribution in the observable \hat{p} associated to the vacuum state is also a gaussian function and that its variance is $\frac{1}{2}$, as in the case of the position-distribution. The product of the two variances is therefore

$$\sigma^2(\hat{q})\sigma^2(\hat{p}) = \frac{1}{4}. \quad (3.5)$$

States which satisfy this equality (instead of inequality 3.4) are said to saturate the uncertainty relation.

This statistical information about the state is encoded, among others, in its Wigner function. The vacuum state belongs to the mentioned class of

¹An ensemble of oscillators is needed because, once observed in a given position the system will start evolving from a position eigenstate and will not behave as $|0\rangle$ any longer, making repeated measurements on the system in the original state impossible. This will be stressed again in chapter 5.

gaussian states, i.e. the states that have a gaussian Wigner function. In particular, the Wigner function for the vacuum is centred on the origin of the phase space and its marginal distributions (as defined in equation 2.4) give the probability densities discussed in this paragraph.

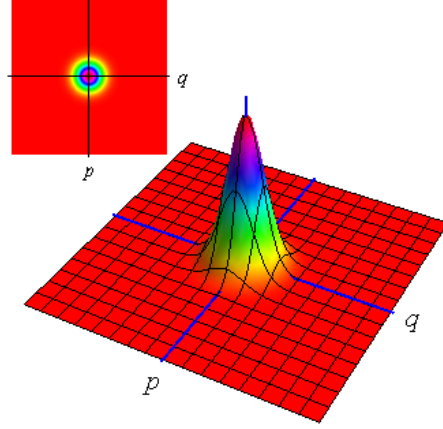


Figure 3.1: Wigner function for the vacuum state $|0\rangle$.

Coherent states

As already anticipated in the introduction to this chapter, coherent states are the closest quantum analogue to classical coherent oscillations (which display harmonically oscillating values for q and p). They can be defined as the eigenstates of the annihilation operator \hat{a} :

$$\hat{a}|\alpha\rangle = \alpha|\alpha\rangle. \quad (3.6)$$

Note that, being \hat{a} non-hermitian, $\alpha \in \mathbb{C}$, while the expectation value of \hat{n} on such states is simply

$$\langle \hat{n} \rangle_{|\alpha\rangle} = \langle \alpha | \hat{a}^\dagger \hat{a} | \alpha \rangle = \alpha^* \alpha = |\alpha|^2.$$

Since $|0\rangle$ satisfies $\hat{a}|0\rangle = 0|0\rangle$, also the vacuum falls within the category of coherent states. Out of the states that have oscillating expectation values for \hat{q} and \hat{p} and saturate the uncertainty relation, coherent states are the ones that have equal intrinsic fluctuations for \hat{q} and \hat{p} , which are

$$\sigma^2(\hat{q}) = \sigma^2(\hat{p}) = \frac{1}{2}.$$

The variance of the number operator \hat{n} for a coherent state is

$$\text{var}(\hat{n}) = \langle \hat{n} \rangle.$$

This is what is generally called, in the case of optical states, *shot noise*. The current output of a photodiode measuring the intensity of an electromagnetic wave is the observable

$$\hat{I} = c\hat{n}.$$

The variance of \hat{I} is, therefore,

$$\text{var}(\hat{I}) = c^2 \text{var}(\hat{n}) = c^2 \langle \hat{n} \rangle = c \langle \hat{I} \rangle.$$

From the above expression the key feature of shot noise becomes evident: it scales linearly with the intensity of the beam impinging on the photodiode.

Coherent states can be expressed, apart from the definition given above, in various ways. For example, they can be written in the basis of number state vectors in the following way:

$$|\alpha\rangle = e^{-\frac{|\alpha|^2}{2}} \sum_{n=0}^{\infty} \frac{\alpha^n}{\sqrt{n!}} |n\rangle.$$

Another expression for a coherent state $|\alpha\rangle$ is

$$|\alpha\rangle = \hat{D}(\alpha)|0\rangle,$$

where the operator $\hat{D}(\alpha)$ is called *displacement* operator and can be written, among other forms, as

$$\hat{D}(\alpha) = e^{\alpha\hat{a}^\dagger - \alpha^*\hat{a}}.$$

The term *displacement* describes the action of this operator on the Wigner function of the vacuum state. In fact, non-vacuum coherent states are described by gaussian $W(q, p)$ with first-moment vector $\bar{R} = (q_0, p_0) \neq 0$. \bar{R} is the vector expressing the average of the quasi-probability distribution and, hence, coherent states have gaussian Wigner functions centred on points different from the origin of the phase space. Since vacuum and coherent states have the same distribution width (or, in more formal terms, the same covariance matrix, as described in section 3.3), $W(q, p)$ for coherent states can be described as a vacuum Wigner function *displaced* to another \bar{R} .

Time evolution in the phase space The time dependence of the expectation values of \hat{q} and \hat{p} can be calculated starting from the coherent state's definition (equation 3.6) and the expression of \hat{q} and \hat{p} as a function of \hat{a} and \hat{a}^\dagger (see appendix A). However, the Wigner phase space-approach provides a more intuitive way to visualize the evolution of a state. In fact, the time evolution operator of H_0 rotates the Wigner function around the origin of the plane, analogously to the classical case, in which a harmonic oscillator is described by a rotating vector in phase space. Therefore, by letting the evolution operator act, the marginal distributions of the Wigner function $|\Psi(q)|^2$ and $|\chi(p)|^2$ will change, with their first moments oscillating between the minimum and maximum value permitted by the amplitude α , as depicted in the following figures.

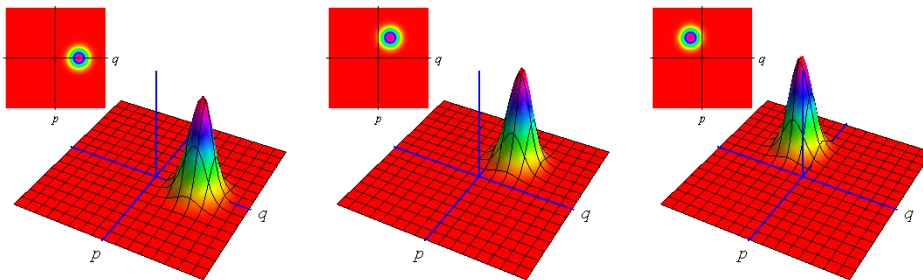


Figure 3.2: Time evolution of a coherent state.

Lattice observables and \hat{q} and \hat{p} It has to be remarked that, in the process of identifying the variables to be taken as position and momentum of the abstract harmonic oscillator (as described at the beginning of section 3.1) a set of normal modes, with different spatial oscillations, is usually available, each having to be quantized separately. The normal modes are generally “rotated” in order to get, for example, (classical) solutions for the position in the form

$$q(\vec{r}, t) \propto e^{i(\vec{k} \cdot \vec{r})}.$$

Such an expression, however, cannot be used to describe the atomic displacements in a lattice. Atomic displacements (and electric fields too) are described by real functions of $\vec{k} \cdot \vec{r}$ (sinusoidal ones) [3]. To recover them from the formalism of the variables q and p , their real (or alternatively, the imaginary) part has to be taken. For example, the atomic displacement \hat{Q}_k can be written as

$$\hat{Q}_k = \hat{a}_k + \hat{a}_{-k}^\dagger.$$

This will be relevant in chapter 4, where some interaction Hamiltonians of vibrational modes in condensed matter with external degrees of freedom will be written using these operators.

3.3 Squeezed states

The vacuum and the coherent states satisfy the saturated uncertainty relation 3.5 in the most simple way possible, and namely with equal $\sigma^2(\hat{q})$ and $\sigma^2(\hat{p})$. However, the Heisenberg relation does not make any request to the distribution of observables taken singularly but only to the product of the variances of two conjugated observables. The fluctuations in one of the two can be therefore reduced (or *squeezed*) to the "damage" of its conjugate, whose fluctuations must be increased in width. States that display such noise properties are called *squeezed states*. However, the term *squeezed* generally refers just to the unbalance in the noise between the two observables, which can exist also for states that do not saturate the uncertainty relation, such as thermal ones. If not specified in more detail, in this thesis the term *squeezed state* will refer to states that saturate the Heisenberg relation.

The squeezing of the distribution of an observable and the corresponding *anti-squeezing* of its conjugate's one are described by the squeezing operator $\hat{S}(\xi)$, defined as follows,

$$\hat{S}(\xi) = e^{\frac{1}{2}(\xi(\hat{a}^\dagger)^2 - \xi^*(\hat{a})^2)}, \quad (3.7)$$

being $\xi = re^{i\psi} \in \mathbb{C}$ the squeezing parameter. A general state of this class can be written as

$$|\alpha, \xi\rangle = \hat{D}(\alpha)\hat{S}(\xi)|0\rangle.$$

In this expression the vacuum state is first squeezed by ξ and then displaced by an amplitude α . This sequence leads to the phase space approach, which a squeezed state is represented in, again, as a gaussian function. However, while coherent and vacuum states have "isotropic" variances in the two axes of the phase space, squeezed states have not. This represents the fact that one of the marginal distributions has been squeezed and the other one adequately anti-squeezed. Figure 3.3 shows an example of such a situation.

In the case represented in figure 3.3, the distribution for \hat{q} is broader than the one for \hat{p} . This means that, in this state, \hat{q} is less determined than \hat{p} is. In order to compactly describe the shape of a gaussian, a part from the first moment vector $\bar{R} = (q_0, p_0)$, we can introduce the covariance matrix, defined as

$$\sigma = \begin{pmatrix} \sigma^2(\hat{q}) & \text{cov}(\hat{q}, \hat{p}) \\ \text{cov}(\hat{p}, \hat{q}) & \sigma^2(\hat{p}) \end{pmatrix}.$$

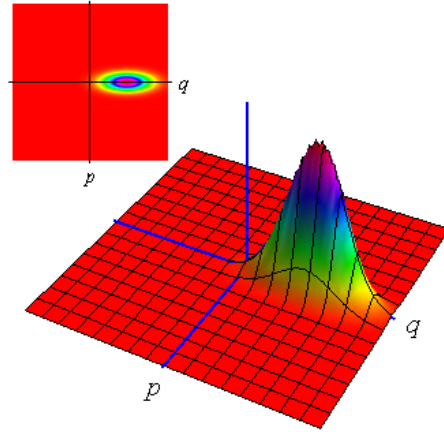


Figure 3.3: Wigner function of a squeezed state.

The state described in the above figure has an associated squeezing parameter with phase $\psi = 0$ and its covariance matrix is diagonal. However, squeezed states can also occur for which the squeezing parameter's phase is non-zero. This would be the case described in figure 3.4. In this case, the covariance

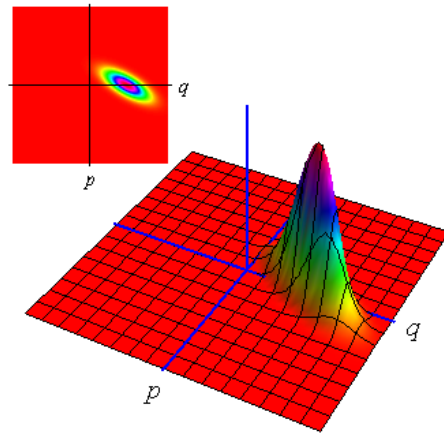


Figure 3.4: Wigner function of a squeezed state with the squeezing parameter's phase $\psi = \frac{5}{3}\pi$.

matrix of the Wigner function is non-diagonal, since it has to account for the correlation between the observables \hat{q} and \hat{p} .

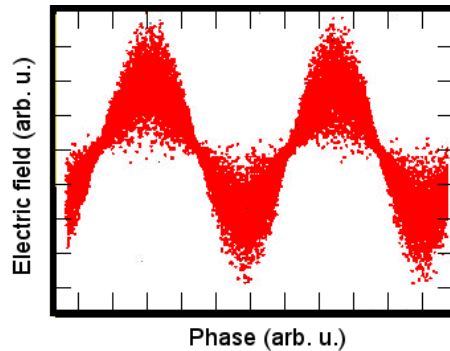


Figure 3.5: The distribution of the electric field of a squeezed optical state. (Image by Gerd Breitenbach, released under CC - attribution, share alike)

To get in more depth into the consequences of such a shape of the Wigner function we will analyse briefly optical squeezed states. The non-trivial statistical properties of optical squeezed states are reflected in the outcomes of phase-resolved measurements of the electric field, e.g. the ones performed with an interferometer. Recalling the time-evolution of the Wigner function described in the previous section, its marginal distribution will have, apart from an oscillating mean value, also an oscillating width, which becomes larger and smaller than the value permitted in a coherent state. In particular, *the variance oscillates at two times the frequency of the mode*. The phase of its oscillation relative to the one of the mean value is determined by the phase ψ of the squeezing parameter ξ . Figure 3.5 shows how repeated phase-resolved measurements of the electric field of a squeezed state look like.

Number and phase squeezed states Depending on the phases where the noise is reduced and the ones where it is increased because of the squeezing, different situations can arise. For example, the noise can be reduced at the nodes of the oscillations. Since the measurement of the phase of an electromagnetic wave is linked to the knowledge of the position of its nodes (or zeros), such state are sometimes called phase-squeezed. They are used, for example, in the gravitational waves-interferometers to have a noise on the measurement of the phase lower than what could be achieved with a coherent optical state. Instead, if the noise is reduced at the extrema of the oscillation, the state is said to be number-squeezed, because the number of photons in the mode is better determined than in the case of a coherent state.

3.4 Thermal states

Thermal states are the states of the harmonic oscillator which present a thermal boson population. This means that the mean number of photons or phonons is given by

$$\langle \hat{n} \rangle = \frac{1}{e^{\beta\omega} - 1}. \quad (3.8)$$

These states describe a harmonic oscillator at equilibrium at a temperature $T = \frac{1}{\beta k_B}$. The density matrix of a thermal state can be written as

$$\hat{\rho}_T = \frac{1}{Z_\beta} e^{-\beta\omega \hat{a}^\dagger \hat{a}}.$$

Its Wigner function is a gaussian centred on the origin of the phase space, as the one of the vacuum state. However, a thermal Wigner function is broader than a vacuum one. This can be intuitively justified observing that the expectation value for the number operator is

$$\langle \hat{n} \rangle = \int dqdp \frac{q^2 + p^2 - 1}{2} W(q, p).$$

If the Wigner function were too sharp, the term containing the parabola $q^2 + p^2$ could not give a contribution to the integral larger than 1. In the case of the vacuum state, its contribution is exactly 1, yielding a number of bosons in the harmonic oscillator which is zero. In the case of a thermal state, instead, it is given by equation 3.8. A broad quasiprobability distribution means also a larger variance, and hence, noise, in the measurement of \hat{q} and \hat{p} . The higher the temperature, the larger the noise. An example of Wigner function for a thermal state is given in figure 3.6. As anticipated in the introduction to this chapter, vibrational modes in condensed matter have energies such that the thermal population of the mode is usually relevant even at room temperature. Therefore, phononic modes at equilibrium must generally be described with thermal states.

Displaced and squeezed thermal states

Acting on a thermal state with a displacement operator produces a displaced thermal state. Despite the term “thermal”, such a state does not describe a system at equilibrium with its surroundings at a given temperature. As for a coherent state, the operators \hat{q} and \hat{p} have oscillating expectation values in a displaced thermal state. Their variance, instead, is larger than the one

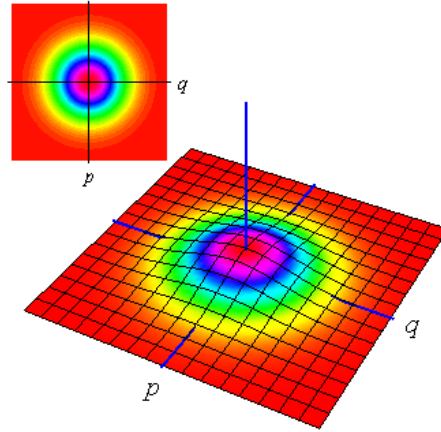


Figure 3.6: Wigner function for a thermal state

for a coherent state and is determined by the original temperature of the “undisplaced” state. In the same way, squeezed thermal states can also occur, which have the phase-dependent variance characteristic of squeezed states.

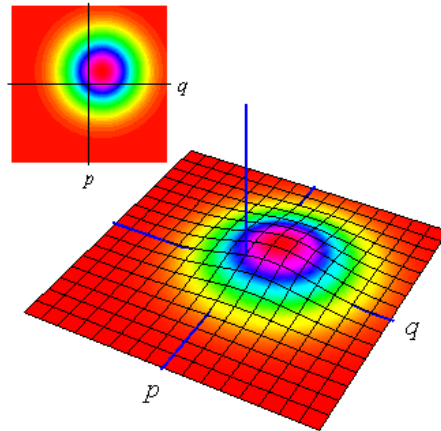


Figure 3.7: Wigner function for a displaced thermal state

Chapter 4

Lowest order light-matter interactions

As already anticipated, some of the interactions of a harmonic oscillator in a gaussian state with external degrees of freedom can be described as simple transformations within the class of gaussian states. The interactions that fall into this category are said to preserve the gaussianity of the state. For what concerns optical modes, they have been extensively studied and experimentally implemented with devices such as lasers, beam-splitters and non-linear optical techniques. They are linear or, at most, bilinear Hamiltonians in the mode operators \hat{a}_k^\dagger and \hat{a}_k and describe, therefore, not only the interactions of a mode with an undefined external source but also mutual interactions of two different modes. In the following, we will first briefly review the situations, which are generally studied in the case of optical states, where the time dependence of the Hamiltonian is very simple, and namely, flat. The interaction in such cases is a constant which is sharply turned on and off as the electromagnetic wave enters and exits the device. Afterwards we will report some less simple cases, relevant to condensed matter. Under some assumptions either on the time-dependence of the Hamiltonian or on the strength of the interaction, its action can still be described in terms of the transformation that preserve the gaussianity of the state. In particular, we will concentrate on impulsive interactions, which are the ones that take place in pump-probe experiments.

4.1 Modes of the electromagnetic field

The most general form for the linear and bilinear Hamiltonians that have a step-like “on and off” time-dependence is [4] (note that the θ time step

functions have been absorbed in the coefficients):

$$H = \sum_k \lambda \hat{a}_k^\dagger + \sum_{k,l} \beta \hat{a}_k^\dagger \hat{a}_l + \sum_{k,l} \zeta \hat{a}_k^\dagger \hat{a}_l^\dagger + h.c. . \quad (4.1)$$

The three building blocks that constitute the above expression give rise to evolution operators that describe simple transformations of a state. In particular, the first term, which is linear in \hat{a}_k^\dagger and \hat{a}_k , corresponds to a displacement operator. This can be, for example, the interaction of an electromagnetic mode with the active medium in a laser.

The second block of 4.1 contains terms of the form $\beta \hat{a}_k^\dagger \hat{a}_l + h.c.$ and describes, instead, interactions that involve linear mixing of two modes. Such processes take place, for example, in a beam-splitter and we will discuss them in some more detail in chapter 5, in the context of the experimental technique called balanced homodyne detection.

Finally, the third block contains the terms $(\hat{a}_k^\dagger)^2 + h.c.$ and $\hat{a}_k^\dagger \hat{a}_l^\dagger + h.c.$, which result in the squeezing of the state. These are the processes that occur, for example, in second-harmonic generation or in an optical parametric amplifier [4].¹ However, only the degenerate form $(\hat{a}_k^\dagger)^2 + h.c.$ gives rise to the single-mode squeezing operator introduced in section 3.3. In the case of the non-degenerate one, the squeezing involves two different modes and the corresponding operator can be expressed as

$$\hat{S}_2(\xi) = e^{\frac{1}{2}(\xi \hat{a}_k^\dagger \hat{a}_l^\dagger - \xi^* \hat{a}_k \hat{a}_l)}. \quad (4.2)$$

A two mode-squeezed state is a state where there is correlation between observables related to the two modes. As an example, two optical beams in the state

$$\hat{S}_2(\xi)|0\rangle \quad (4.3)$$

are called twin-beams [4]. In this state there is perfect correlation between the photon numbers in the two modes, i.e. the difference between the number of photons in the two modes is a constant of motion.²

¹Note that only two modes appear in these two expressions. In the case of the mentioned non-linear optical processes, they are the output photon modes. The input photon operators have been absorbed in the coefficients.

²Note that, here, $|0\rangle$ denotes the state $|0\rangle_k \otimes |0\rangle_l$, where k and l are the two modes involved in the squeezing.

4.2 Light-matter interaction and the generation of quantum phonon states

The main goal of this project goes beyond the description of the evolution of optical states by themselves. It focuses on the description of processes occurring in condensed matter and their interaction with optical states, i.e. light. In this section we will concentrate on two possible mechanisms involved in the excitation of the vibrational states which have usually been dubbed as “coherent phonons”. This term, though, was originally meant with the classical meaning of *coherence* as phase-coherence in an oscillation and not in the quantum one which has been described in chapter 3.

In the following, we will analyse two possible excitation mechanisms which generate coherent and two mode-squeezed vibrational states. It has furthermore to be considered that, as already mentioned at the beginning of this chapter, phonons do not evolve freely but strongly interact with the surrounding environment. The state of a vibrational mode is thus not determined just by its excitation but also by its subsequent evolution.

In order to avoid confusion in the discussion of photonic and phononic states together, in this chapter we will adopt the general convention, in which the operators \hat{a}^\dagger and \hat{a} refer to the modes of the electromagnetic field, while \hat{b}^\dagger and \hat{b} refer to the vibrational ones.

Generation of coherent phonons - linear coupling

A vibrational mode can be excited in a coherent state when it is coupled to external degrees of freedom through a Hamiltonian which is linear in the mode operators \hat{b}^\dagger and \hat{b} [2]. In fact, this is the case of the first block of Hamiltonian 4.1. When the time-dependence of the Hamiltonian is simple (either “flat”, as in the previous section, or impulsive, as we will discuss later) its evolution transformation is directly a displacement operator. It can be shown, however, that this is true for a general time-dependence of the Hamiltonian if the initial state is a vacuum state or a coherent one.

Let us consider the following Hamiltonian:

$$\hat{H}(t) = \Omega \hat{b}^\dagger \hat{b} + \lambda(t) \hat{b}^\dagger + \lambda^*(t) \hat{b}. \quad (4.4)$$

In the Heisenberg picture, the operator \hat{b} evolves according to

$$\begin{aligned}
\dot{\hat{b}} &= i[\hat{H}(t), \hat{b}] \\
&= i\{\Omega[\hat{b}^\dagger \hat{b}, \hat{b}] + \lambda(t)[\hat{b}^\dagger, \hat{b}] + \lambda^*(t)[\hat{b}^\dagger, \hat{b}]\} \\
&= i\{\Omega\hat{b}^\dagger[\hat{b}, \hat{b}] + \Omega[\hat{b}^\dagger, \hat{b}]\hat{b} - \lambda(t)\} \\
&= -i\Omega\hat{b} - i\lambda(t).
\end{aligned} \tag{4.5}$$

This equation can be integrated to give

$$\begin{aligned}
\hat{b}(t) &= e^{-i\Omega t}\hat{b} + \int_{-\infty}^t ds e^{-i\Omega(t-s)}\lambda(s) \\
&= e^{-i\Omega t}\hat{b} + e^{-i\Omega t} \int_{-\infty}^t ds e^{i\Omega s}\lambda(s) \\
&= e^{-i\Omega t}(\hat{b} + \Lambda(t)),
\end{aligned} \tag{4.6}$$

where

$$\Lambda(t) = \int_{-\infty}^t ds e^{i\Omega s}\lambda(s). \tag{4.7}$$

An initial coherent state $|\beta\rangle$ is³, before the interaction, an eigenstate of the operator \hat{b} with an eigenvalue β :

$$\hat{b}|\beta\rangle = \beta|\beta\rangle. \tag{4.8}$$

When the interaction takes place, \hat{b} starts evolving. However, an initially coherent state remains an eigenstate of $\hat{b}(t)$, with the new eigenvalue $e^{-i\Omega t}(\beta + \Lambda(t))$.

$$\begin{aligned}
\hat{b}(t)|\beta\rangle_0 &= e^{-i\Omega t}(\hat{b} + \Lambda(t))|\beta\rangle_0 \\
&= e^{-i\Omega t}(\beta + \Lambda(t))|\beta\rangle_0
\end{aligned} \tag{4.9}$$

Therefore, such an interaction can excite a coherent vibrational state (in the quantum sense) if the initial state of the mode is, for example, the vacuum:

$$|\beta\rangle_0 \rightarrow |e^{-i\Omega t}(\beta + \Lambda(t))\rangle. \tag{4.10}$$

Note that $\Lambda(t)$ is related to the Fourier-component of $\lambda(t)$ at the frequency of the phonon mode.

³For the vacuum state, $\beta = 0$.

If the interaction is impulsive, we can write a more general result [2], which applies to any initial state the mode is in.⁴ In this case, the time-dependence $\lambda(t)$ can be written as

$$\lambda(t) = l\delta(t - t_0). \quad (4.11)$$

The interaction picture-evolution operator is

$$\begin{aligned} \hat{U}_I(t) &= 1 - i \int_{-\infty}^t ds (l\delta(s - t_0)\hat{b}_I^\dagger + l^*\delta(s - t_0)\hat{b}_I) \\ &\quad + (-i)^2 \int_{-\infty}^t ds_1 \int_{-\infty}^{s_1} ds_2 \{ (l\delta(s_1 - t_0)\hat{b}_I^\dagger + l^*\delta(s_1 - t_0)\hat{b}_I) \cdot \\ &\quad \cdot (l\delta(s_2 - t_0)\hat{b}_I^\dagger + l^*\delta(s_2 - t_0)\hat{b}_I) \} \\ &\quad + \dots \\ &= 1 - i \int_{-\infty}^t ds (l\delta(s - t_0)\hat{e}^{i\Omega s}b^\dagger + l^*\delta(s - t_0)\hat{e}^{-i\Omega s}b) \\ &\quad + (-i)^2 \int_{-\infty}^t ds_1 \int_{-\infty}^{s_1} ds_2 \{ (l\delta(s_1 - t_0)\hat{e}^{i\Omega s_1}b^\dagger + l^*\delta(s_1 - t_0)e^{-i\Omega s_1}\hat{b}) \cdot \\ &\quad \cdot (l\delta(s_2 - t_0)\hat{e}^{i\Omega s_2}b^\dagger + l^*\delta(s_2 - t_0)e^{-i\Omega s_2}\hat{b}) \} \\ &\quad + \dots \\ &= e^{-i(l e^{i\Omega t_0}\hat{b}^\dagger + l^* e^{-i\Omega t_0}\hat{b})}. \end{aligned} \quad (4.12)$$

$\hat{U}(t)$ becomes, in the Schrodinger picture,

$$\hat{U}(t) = e^{-i\Omega t\hat{b}^\dagger\hat{b}} e^{-i(l e^{i\Omega t_0}\hat{b}^\dagger + l^* e^{-i\Omega t_0}\hat{b})}. \quad (4.13)$$

The second factor in the above expression is exactly the displacement operator $\hat{D}(\Lambda)$ with

$$\Lambda = \frac{l}{i} e^{i\Omega t_0}.$$

Therefore, given a general initial state $\hat{\rho}_i$, the final state $\hat{\rho}_f$ after a linear impulsive interaction is

$$\hat{\rho}_f = \hat{D}^\dagger(\Lambda)\hat{\rho}_i\hat{D}(\Lambda), \quad (4.14)$$

⁴It is worth stressing that the couplings which are described by these Hamiltonians are not necessarily direct interactions of the vibrational modes and the electromagnetic field. In fact, the symmetry of the phonon mode considered in this thesis (chapter 7) does not allow an electric-dipole interaction with an electromagnetic field, which would be the linear interaction with light. Such a coupling should therefore be mediated. In particular, in the case of Bismuth, it is mediated by electrons.

which then freely evolves.

The most natural initial state for a vibrational mode at thermal equilibrium is a thermal one. With such an initial state, this kind of interaction produces a displaced thermal state

$$\hat{\rho}_f = \hat{D}^\dagger(\Lambda)\hat{\rho}_T\hat{D}(\Lambda), \quad (4.15)$$

as depicted in figure 4.1.

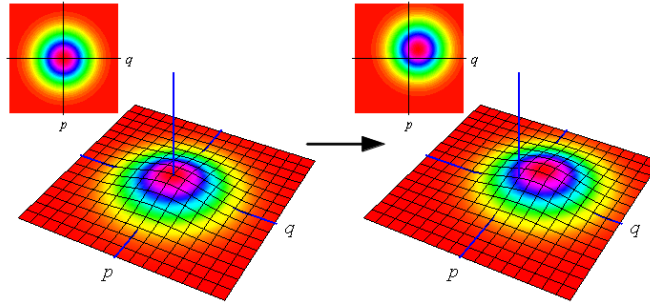


Figure 4.1: Displacement of a thermal state via a linear interaction with an external source.

Generation of squeezed phonons - bilinear/quadratic coupling

As already shown in the case of optical states, squeezing occurs when bilinear interactions of the modes are present in the form $\hat{b}_k^\dagger\hat{b}_l^\dagger + \text{h.c.}$. These are interactions in which two different vibrational modes are coupled or which are quadratic in the operators of a single mode. They are always relevant for vibrational modes in a solid, since, even not considering the interaction with light, many vibrational modes are present and they interact one with another. Considering instead the case of the interaction of condensed matter with light, a Hamiltonian which is bilinear in the phononic modes operators describes, for example, what is called second-order Raman scattering [2]. In particular, the stimulated Raman scattering is a process which is linked to the third-order susceptibility of the solid, when it is expanded in powers of the electric field. Here, second-order refers to the term in the expansion of the susceptibility in the atomic displacements. This interaction involves the simultaneous creation (or annihilation) of two phonons in two vibrational modes with opposite crystal momentum k . However, second-order Raman scattering is only one out of the interactions that produce squeezed states in condensed matter. In fact,

the necessary factors of the interaction Hamiltonian are only the ones in the form $\hat{b}_k^\dagger \hat{b}_l^\dagger + \text{h. c.}$.

Let us consider first of all the case in which the interaction Hamiltonian contains only bilinear terms in the mode operators. In this situation, the evolution operator is a two-mode squeezing one. It has been shown [5] that if both linear and bilinear terms involving a mode appear in the Hamiltonian, the evolution operator can still be factorized in a displacement and a squeezing one, with the introduction of an additional global phase factor. Considering only the bilinear part, the total Hamiltonian can be written in the form

$$\begin{aligned} \hat{H}_{k_1, k_2} = & \Omega_{k_1} \hat{b}_{k_1}^\dagger \hat{b}_{k_1} + \Omega_{k_2} \hat{b}_{k_2}^\dagger \hat{b}_{k_2} + \\ & + \zeta(t) \hat{b}_{k_1}^\dagger \hat{b}_{k_2}^\dagger + \zeta^*(t) \hat{b}_{k_1} \hat{b}_{k_2}, \end{aligned} \quad (4.16)$$

where k_1 and k_2 are the momenta of the two modes we are considering, $\zeta(t)$ is a general function of time and Ω_{k_1} and Ω_{k_2} are the frequencies of the two modes. \hat{H} consists of a free part,

$$\hat{H}_0 = \Omega_{k_1} \hat{b}_{k_1}^\dagger \hat{b}_{k_1} + \Omega_{k_2} \hat{b}_{k_2}^\dagger \hat{b}_{k_2}, \quad (4.17)$$

and an interaction one,

$$\hat{H}_1 = \zeta(t) \hat{b}_{k_1}^\dagger \hat{b}_{k_2}^\dagger + \zeta^*(t) \hat{b}_{k_1} \hat{b}_{k_2}. \quad (4.18)$$

In order to retrieve a simple phase-space transformation from the evolution operator of this Hamiltonian with a general time-dependence, $\zeta(t)$ must be small. In the impulsive case, instead, using the same procedure as in the previous section, the result is exact.

In the small $\zeta(t)$ case, the Dyson series can be truncated to the first order in $\zeta(t)$, as shown below in the interaction picture.

$$\begin{aligned} \hat{U}(t) = & 1 - i \int_{-\infty}^t ds \hat{H}_1(s) + \dots \\ \simeq & 1 - i \int_{-\infty}^t ds \hat{H}_1(s) \end{aligned} \quad (4.19)$$

This last expression can be approximated as

$$\hat{U}(t) \simeq e^{-i \int_{-\infty}^t ds \hat{H}_1(s)}. \quad (4.20)$$

Using the explicit expression for $H_1(t)$ we retrieve a two-mode squeezing operator with a time dependent squeezing parameter:

$$\begin{aligned}\hat{U}_{k_1, k_2}(t) &\simeq e^{-i \int_{-\infty}^t ds \left(\zeta(t) \hat{b}_{k_1}^\dagger \hat{b}_{k_2}^\dagger e^{i(\Omega_{k_1} + \Omega_{k_2})t} + \zeta^*(t) \hat{b}_{k_1} \hat{b}_{k_2} e^{i(\Omega_{k_1} + \Omega_{k_2})t} \right)} \\ &= e^{-i \left(\xi(t) \hat{b}_{k_1}^\dagger \hat{b}_{k_2}^\dagger + \xi^*(t) \hat{b}_{k_1} \hat{b}_{k_2} \right)} \\ &= \hat{S}_2(\xi(t)),\end{aligned}\tag{4.21}$$

where

$$\xi(t) = \int_{-\infty}^t ds \zeta(t) e^{i(\Omega_{k_1} + \Omega_{k_2})t}.\tag{4.22}$$

As already mentioned, for what concerns the vibrational modes, (stimulated) second-order Raman scattering is an interaction of this kind. Generally, the Hamiltonian for the coupling of a dipole (which in our case is the solid's polarization) is in the following form:

$$\begin{aligned}\hat{H}_E &= -\bar{P} \cdot \bar{E} \\ &= -P_\mu E_\mu\end{aligned}\tag{4.23}$$

while the n-th order polarization in the electric field is

$$P_\mu^{(n)} = \epsilon_0 X_{\mu\nu}^{(n)} E_\nu,\tag{4.24}$$

where $X_{\mu\nu}^{(n)}$ is the n-th order susceptibility. Stimulated Raman scattering is a non-linear effect due to $X^{(3)}$, which is given by

$$X_{\mu\nu}^{(3)} = \chi_{\mu\nu, \alpha\beta}^{(3)} E_\alpha E_\beta.\tag{4.25}$$

The interaction Hamiltonian is therefore

$$\hat{H}_E^{(R)} = \chi_{\mu\nu, \alpha\beta}^{(3)} E_\alpha E_\beta E_\nu E_\mu.\tag{4.26}$$

We can now expand the solid's susceptibility $\chi_{\mu\nu, \alpha\beta}^{(3)}$ in powers of the atomic displacements. If we consider only the modes $+k$ and $-k$ to interact, we can consider just the terms which couple the atomic displacements for these two modes. Taking the second-order terms we obtain

$$\hat{H}_E^{(R)} \propto Q_{k\alpha} Q_{-k\beta} E_\alpha E_\beta E_\nu E_\mu\tag{4.27}$$

Considering the atomic displacements on the same axis, $\hat{H}_E^{(R)}$ can be written as

$$\hat{H}_E^{(R)} = Z(t) Q_k Q_{-k},\tag{4.28}$$

where $Z(t)$ contains the electric fields and other proportionality terms. Considering now the vibrational modes as quantized, the atomic displacements can be written using the creation and annihilation operators of the modes as follows

$$Q_k = \hat{b}_k + \hat{b}_{-k}^\dagger. \quad (4.29)$$

Therefore, the bilinear interaction Hamiltonian of the modes $+k$ and $-k$ becomes

$$\begin{aligned} \hat{H}_E^{(R)} &= Z(t)(\hat{b}_k + \hat{b}_{-k}^\dagger)(\hat{b}_{-k} + \hat{b}_k^\dagger) \\ &= Z(t)(\hat{b}_k^\dagger \hat{b}_k + \hat{b}_{-k}^\dagger \hat{b}_{-k} + 1) + \underbrace{Z(t)(\hat{b}_k \hat{b}_{-k} + \hat{b}_k^\dagger \hat{b}_{-k}^\dagger)}_{\text{underlined}}. \end{aligned} \quad (4.30)$$

The underlined term is the one needed to produce the squeezing.

Going, again, to the impulsive case, i.e. the situation in which

$$Z(t) = z\delta(t), \quad (4.31)$$

$\hat{U}(t)$ is

$$\hat{U}(t) = e^{-i\hat{H}t/\hbar} e^{iz(\hat{b}_k^\dagger \hat{b}_k + \hat{b}_{-k}^\dagger \hat{b}_{-k})} \underbrace{e^{\xi \hat{b}_k^\dagger \hat{b}_{-k}^\dagger - \xi^* \hat{b}_k \hat{b}_{-k}}}_{\hat{S}_2(\xi)} \quad (4.32)$$

Therefore, impulsive second-order Raman scattering produces a two-mode squeezed state with a squeezing parameter

$$\xi = iz e^{-iz}.$$

Chapter 5

Quantum state reconstruction - Tomography

Having discussed some of the interactions of a harmonic oscillator, the point is now how to discover, given such a system, its state when it is unknown. More in general, what does it mean to “*measure* the quantum state of a system”? The task of experimentally determining the state of a system is called *quantum tomography*. It consists in gathering all the information needed, together with physical laws, to be able to predict the behaviour of the system in future experiments. This means to predict the statistical distributions of the outcomes of all possible measurements it can be performed upon. The fundamental object which this information is encoded in is the density matrix $\hat{\rho}$. Quantum tomography is therefore the experimental process in which the density matrix is reconstructed. It is worth stressing that, while the state of a classical system can be determined by performing repeated measurements on it, the knowledge of the state of a system which must be described with quantum mechanics is not accessible, in general, when a single copy of the system itself is available. In fact, the very act of measuring an observable of the system changes its state, making repeated measurements on it meaningless towards the determination of its initial state. Therefore, quantum tomography is only possible when an ensemble of identically prepared systems is available. With such an ensemble, repeated measurements are possible, each of them independently performed on a different copy. Furthermore, as recognized for the first time by Fano [1], in order to have enough information to fully reconstruct the density matrix, it proves necessary to measure a set, called *quorum*, of at least two non-commuting observables \hat{O}_i . This allows to estimate all the

matrix elements ρ_{ij} of the density matrix (represented in a basis $\{|\phi_i\rangle\}$),

$$\rho_{ij} = \langle \phi_i | \hat{\rho} | \phi_j \rangle.$$

A more detailed example of this in the case of a two-level system is discussed in appendix B.

While the tomography of optical states is routinely performed in quantum optics laboratories, it is not used in the context of condensed matter. The goal of this project is to develop the theoretical and experimental tools for the characterization of states in condensed matter, e.g. the ones of a vibrational mode. Being optical tomography a well established technique, the most natural question and goal of this project is whether we can study quantum states in a solid, and in particular coherent ones, by characterizing the state of light pulses after their interaction with the material. However, it is possible to study states in condensed matter even in other ways. In chapter 6 we will present experimental set-ups we have built to measure the properties of the quantum state of the excitations induced in a solid in pump-probe experiments.

Instead, in this chapter we will describe the standard technique used in quantum optics to perform the tomography of optical states, balanced homodyne detection. The origins of its use in this context date back to 1993 [6] and it has been extensively developed since then. Balanced homodyne detection is an experimental scheme that gives access to the measurement of the quadratures of an electromagnetic field mode. From the expressions for the two basic ones,

$$\hat{q} = \frac{1}{\sqrt{2}}(\hat{a} + \hat{a}^\dagger)$$

$$\hat{p} = \frac{1}{i\sqrt{2}}(\hat{a} - \hat{a}^\dagger),$$

a generalization can be drawn, in the form

$$\hat{x}_\Phi = \frac{1}{\sqrt{2}}(\hat{a}e^{-i\Phi} + \hat{a}^\dagger e^{i\Phi}).$$

These quantities are of interest because the set of all the quadratures with Φ spanning the interval $[0, 2\pi]$ constitutes a quorum for the state of a harmonic oscillator and, hence, also for optical states. By performing repeated measurements of the quadrature *at a given phase* Φ , the probability distributions $p_\Phi(x)$ of obtaining the value x in the measurement of the observable \hat{x}_Φ can be

estimated. This is possible since the histograms of the data collected approach the actual form of $p_\Phi(x)$ as the number of data increases. Since

$$p_\Phi(x) = \text{Tr}(|x_\Phi\rangle\langle x_\Phi|\hat{\rho}), \quad (5.1)$$

the question now is whether this equation can be inverted in order to estimate $\hat{\rho}$ from the collected data (x, Φ) and their histograms. The Wigner function equivalents of equation 5.1 for $\hat{x}_0 = \hat{q}$ and $\hat{x}_{\frac{\pi}{2}} = \hat{p}$ are its marginal distributions $|\Psi(q)|^2$ and $|\chi(p)|^2$ introduced in chapter 2. They could be rewritten as $p_{\Phi=0}(x)$ and $p_{\frac{\pi}{2}}(x)$ respectively. In order to get the distribution for a general quadrature \hat{x}_Φ , the marginal distribution of the Wigner function must be taken integrating on an axis rotated by $\Phi - \frac{\pi}{2}$ with respect to q . Upon a change of variables the integral becomes [7]:

$$p_\Phi(x) = \int_{-\infty}^{+\infty} dy W(x \cos \Phi - y \sin \Phi, x \sin \Phi + y \cos \Phi). \quad (5.2)$$

This expression is what is known as Radon transform of the function $W(x, y)$, which in this case is the Wigner function.¹ The latter can be therefore recovered by taking the Radon anti-transform of the measured $p_\Phi(x)$. However, the full reconstruction of the Wigner function or of the density matrix is not a necessary step. Functions can be derived, called *kernel* or *pattern* functions [8, 9, 10], which allow to directly calculate the expectation values of observables bypassing the explicit reconstruction of $W(q, p)$. They are written in order for the expectation value $\langle \hat{O} \rangle$ to be a simple average of its pattern function $R[\hat{O}](x, \Phi)$ weighted with the estimated probability densities $p(x, \Phi)$:

$$\langle \hat{O} \rangle = \int_0^{2\pi} \frac{d\Phi}{\pi} \int_{-\infty}^{+\infty} dx p(x, \Phi) R[\hat{O}](x, \Phi).$$

5.1 Balanced homodyne detection

The experimental set-up that allows to measure the quadratures of optical states is called, as already mentioned, balanced homodyne detector. Its core is depicted in figure 5.1.

The scheme depicted in figure 5.1 is the upper part of a Mach-Zehender interferometer, in which an incoming beam is split in two and then recombined on a 50-50 beam-splitter as shown above. In such an interferometer, according to

¹As a historical remark, the term tomography originates from the similarity of this technique and the one used in medical context, where the Radon transform found one of its earliest applications.

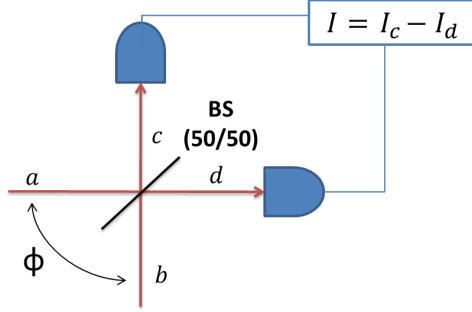


Figure 5.1: Basic scheme of a balanced homodyne detector

the phase-difference between the two beams a and b , the reflectivity and the transmittance of the beam-splitter can be tuned, up to forcing all the light to go either way or the other. This happens because, depending on their phase difference, the two beams constructively and destructively interfere, respectively, on the two sides of the beam-splitter.

Balanced homodyne detection involves two different beams of light. The first one, which is usually termed *signal* (and which we take to be a in figure 5.1), is the beam constituted by the mode in the state $\hat{\rho}_s$. Its state has been prepared in an unknown way and is the one that has to be studied. The second one, called *local oscillator* (b in figure 5.1), is in a coherent state $|z\rangle\langle z|$ and is used as a reference. Its role is to tune the phase Φ of the quadrature to be measured. The two beams are mixed, as shown in figure 5.1 on a 50-50 beam-splitter. Their interaction can be described, as briefly discussed in chapter 4, by a Hamiltonian of the form

$$H_{BS} = \beta \hat{a}^\dagger \hat{b} + \text{h. c. .}$$

Here \hat{a} is the annihilation operator of the signal mode and \hat{b} is the one of the local oscillator². This kind of Hamiltonian leads to the evolution operator

$$\hat{U}_{BS}(\eta) = e^{\eta \hat{a}^\dagger \hat{b} - \eta^* \hat{a} \hat{b}^\dagger},$$

where $\eta = |\eta|e^{i\delta}$ is proportional to the interaction time (i.e. to the length of the path of the beams within the beam-splitter) and to the linear susceptibility of the medium the beam-splitter is made of [4]. Denoting with \hat{c} and \hat{d} the operators describing the modes *after* the beam-splitter (or, as said in quantum

²In this chapter \hat{a} , \hat{b} , \hat{c} and \hat{d} all refer to optical states.

optics, in its output ports), the evolution of the operators \hat{a} and \hat{b} under this interaction is

$$\begin{pmatrix} \hat{c} \\ \hat{d} \end{pmatrix} = \hat{U}_{BS}^\dagger(\eta) \begin{pmatrix} \hat{a} \\ \hat{b} \end{pmatrix} \hat{U}_{BS}(\eta),$$

which can be rewritten as

$$\hat{B}(\eta) \begin{pmatrix} \hat{a} \\ \hat{b} \end{pmatrix} = \begin{pmatrix} \cos(|\eta|) & e^{i\delta} \sin(|\eta|) \\ -e^{i\delta} \sin(|\eta|) & \cos(|\eta|) \end{pmatrix} \begin{pmatrix} \hat{a} \\ \hat{b} \end{pmatrix}.$$

In the case of a 50-50 beam-splitter, $\eta \in \mathbb{R}$ and equals $\frac{\pi}{4}$ and the transformation reads simply

$$\begin{pmatrix} \hat{c} \\ \hat{d} \end{pmatrix} = \begin{pmatrix} \frac{1}{\sqrt{2}}(\hat{b} + \hat{a}) \\ \frac{1}{\sqrt{2}}(\hat{b} - \hat{a}) \end{pmatrix}. \quad (5.3)$$

The phase between the signal and the local oscillator on the beam-splitter can be varied by changing the optical path of the local oscillator, generally done by moving a mirror mounted on a *piezo*-translator. This phase-shift can be described by the following transformation of the mode operators of the local oscillator:

$$\begin{pmatrix} \hat{b} \\ \hat{b}^\dagger \end{pmatrix} = \begin{pmatrix} e^{i\Phi} \hat{b} \\ e^{-i\Phi} \hat{b}^\dagger \end{pmatrix}. \quad (5.4)$$

The intensity of the beams in the output ports of the beam-splitter is then detected by two photodiodes C and D. The difference I between the currents I_c and I_d produced in the two photodiodes is amplified and acquired. The photo-current observables \hat{I}_c and \hat{I}_d are proportional to the photon numbers in the two beams, $\hat{n}_c = \hat{c}^\dagger \hat{c}$ and $\hat{n}_d = \hat{d}^\dagger \hat{d}$. As we will discuss later, there is a particular measurement that can be used to define the units of the observables involved in this kind of experiment and we can therefore put the proportionality factor between \hat{I} and \hat{n} to 1. Hence, the difference \hat{I} between the photocurrents is

$$\hat{I} = \hat{n}_c - \hat{n}_d = \hat{c}^\dagger \hat{c} - \hat{d}^\dagger \hat{d}.$$

It turns out that, under two conditions on the intensities of the signal and local oscillator beams, the difference current observable \hat{I}_Φ at a given local oscillator phase Φ is proportional to the quadrature observable \hat{x}_Φ .

In fact, taking into account the transformation due to the beam-splitter (5.3) and the one due to the phase-shifting of the local oscillator (5.4), the difference current can be rewritten as

$$\hat{I}_\Phi = \hat{a}^\dagger \hat{b} e^{i\Phi} + \hat{b}^\dagger e^{-i\Phi} \hat{a}.$$

Its expectation value is proportional to the expectation value of \hat{x}_Φ , as demonstrated in the following lines:

$$\begin{aligned}
 \langle \hat{I}_\Phi \rangle &= \text{Tr} (\hat{I}_\Phi \hat{\rho}_s \otimes |z\rangle\langle z|) = \text{Tr} ((\hat{a}^\dagger \hat{b} e^{i\Phi} + \hat{b}^\dagger e^{-i\Phi} \hat{a}) \hat{\rho}_s \otimes |z\rangle\langle z|) \\
 &= \text{Tr} (\hat{a}^\dagger \hat{b} e^{i\Phi} \hat{\rho}_s \otimes |z\rangle\langle z|) + \text{h. c.} = \text{Tr} (\hat{a}^\dagger \hat{\rho}_s) \text{Tr} (\hat{b} e^{i\Phi} |z\rangle\langle z|) + \text{h. c.} \\
 &= \text{Tr} (\hat{a}^\dagger \hat{\rho}_s) \langle z | \hat{b} e^{i\Phi} |z\rangle + \text{h. c.} = \text{Tr} (\hat{a}^\dagger \hat{\rho}_s) |z| e^{i\Phi} + \text{h. c.} \\
 &= |z| \text{Tr} ((\hat{a}^\dagger e^{i\Phi} + \hat{a} e^{-i\Phi}) \hat{\rho}_s) \\
 &= \sqrt{2} |z| \text{Tr} (\hat{x}_\Phi \hat{\rho}_s) = \sqrt{2} |z| \langle \hat{x}_\Phi \rangle.
 \end{aligned} \tag{5.5}$$

The above calculation must, however, be accompanied by a condition which ensures that the difference current's spectrum, which is discrete (being the difference of two number operators) well approximates the continuous spectrum of the quadratures \hat{x}_Φ . This condition is that

$$|z| \gg 1.$$

It means that the local oscillator must be very intense. Nevertheless, in order to have access to the probability densities $p_\Phi(x)$, the observables \hat{I}_Φ and \hat{x}_Φ must also have, a part from equal expectation values, also equal distributions. In other words, all their statistical moments must coincide. As an example, the second-order moment of the difference current (which has been divided by the factor $\sqrt{2}|z|$ derived in equation 5.5) is

$$\begin{aligned}
 \frac{\hat{I}_\Phi}{\sqrt{2}|z|} &= \frac{1}{\sqrt{2}|z|} \text{Tr} ((\hat{a}^\dagger \hat{b} e^{i\Phi} + \hat{a} \hat{b}^\dagger e^{-i\Phi}) \hat{\rho}_s \otimes |z\rangle\langle z|) \\
 &= \langle \hat{x}_\Phi^2 \rangle + \left\langle \frac{\hat{a}^\dagger \hat{a}}{2|z|^2} \right\rangle.
 \end{aligned} \tag{5.6}$$

The condition for the second moments of the observables to coincide, a part from the proportionality factor, is therefore that

$$|z|^2 \gg \langle \hat{a}^\dagger \hat{a} \rangle_{\hat{\rho}_s} = \langle \hat{n} \rangle_{\hat{\rho}_s}. \tag{5.7}$$

Hence, not only the local oscillator has to be intense, but it has to be much more intense than the signal beam. This can be referred to as a quantum regime of the Mach-Zehender interferometer, opposed to a classical one in which the signal field is in a large-amplitude coherent state. We will discuss the latter case in more detail in section 6.4, in the context of an experimental technique we have developed.

It can furthermore be proven that condition 5.7 ensures that even all the higher order moments of \hat{I}_Φ and \hat{x}_Φ are equivalent.

Vacuum measurement - Defining the units As mentioned, there is a particular measurement that allows to calibrate the detector defining a unit in the values of the difference current. This is the measurement of the distributions $p_\Phi(x)$ for the vacuum state. In fact, the variance of the distribution of the quadratures for a vacuum state is $\frac{1}{2}$ for all the values of Φ and provides a rescaling factor to be applied to the data. The measurement can be performed blocking the signal beam before it enters the beam-splitter, therefore preparing the signal beam in the vacuum state.

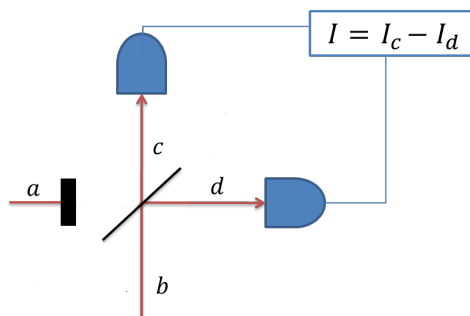


Figure 5.2: Vacuum measurement

Technical notes on the detection system The measurements of the photo-current, which corresponds to the number of photons, will display some amount of noise, generated by different sources. A contribution to the total noise comes directly from the state, as described in chapter 3, and is called *shot noise*. The shot-noise power of a coherent state linearly increases with the intensity of the beam hitting a photo-diode and it is not a property of the detector, while the rest of the noise, called *electronic noise*, is. Shot noise is the one that we are interested in for the measurement of the distributions $p_\Phi(x)$. Therefore, in order for the latter to be meaningful, the shot noise must be the dominant one in the measurement process. A useful parameter, to compare shot and electronic noise with, is the so-called *shot-to-electronic noise ratio*, i.e. the signal-to-noise ratio in the case of a vacuum measurement. The higher this ratio is, the better the measurement of $p_\Phi(x)$.

The relation between the distributions \hat{I} and \hat{x}_Φ not only is bound to the condition of low electronic noise but to a high efficiency η of the photo-diode too. In fact, while for $\eta = 1$ the correspondence between the two is perfect, it progressively becomes less reliable when η decreases. (see [11])

Another fundamental property of the detection system to know, is the light-

intensity interval in which it is in its linear regime. It is the regime in which the photo-current linearly increases with the intensity of the light impinging on the photo-diode. Out of this interval (which extends from 0 up to a certain intensity) the photo-current cannot be considered proportional to the photon-number any more, since the relation between the two is not linear.

Moreover, the detector must be highly efficient in the subtraction of the signals from the two photo-diodes.

The characterization of the parameters of our set-up for balanced homodyne detection will be discussed in chapter 6.

Pulsed regime The above discussion takes into account two beams which are continuous waves. However, the use of beams produced by pulsed lasers is of much more general interest. It opens up the possibility to exploit the non-linear optical properties of materials and allows to perform time-resolved pump-probe measurements.

In order to describe a pulsed beam, more than a single mode of the electromagnetic field has to be considered. Nevertheless, it can be shown [12] that balanced homodyne detection in the pulsed regime still measures the quadratures of the generalized mode describing the signal beam, upon the following redefinition of its mode operators:

$$\hat{A}^\dagger(\bar{\alpha}) = \sum_l \alpha_l \hat{a}_l^\dagger.$$

A part from the above mentioned formal adjustments, some technical issues arise in this context. With a pulsed beam the values of the difference current are acquired and numerically integrated separately over the time interval corresponding to a single pulse. These integrals are the numbers associated to the measurements of the quadratures. Therefore, the detector electronics must be fast enough to avoid the overlap of successive pulses in order to measure single pulse properties. Moreover, the requirements of a high shot-to-electronic noise ratio and of a high subtraction efficiency have to be met on all the frequency range that goes from DC up to the repetition rate of the pulses in the beam.

Chapter 6

The experimental set-up

The goal of the project this thesis is set in is to extend to condensed matter the concepts underlying the quantum tomography of optical states. The phenomena which we are interested in are transient states produced in pump-probe experiments, e.g. the coherent phononic vibrations in Bismuth, and the techniques which we are about to describe naturally involve extended pump-probe set-ups.

In a pump-probe experiment the sample under study is excited with an intense ultra-short laser pulse, dubbed pump. The variation of the optical properties of the sample, e.g. its reflectivity, are studied with a second ultra-short light pulse, which is called probe. By changing the time-delay between the excitation with the pump pulse and the probing with the probe pulse it is possible to study the temporal evolution of the optical properties of the solid after the excitation. Pump-probe experiments are most commonly performed using quasi-monochromatic light pulses centred at a wavelength of 800 nm.¹ However, different approaches are becoming more and more common.

The task of studying quantum states in condensed matter can be approached from various angles. Being optical tomography a well established technique, the main direction of the project is to study how the state of a light pulse is affected by the interaction with a material and, in particular, with a sample out of equilibrium. The information about the sample dynamics which is encoded in the probe's state can be retrieved via optical tomography. The first section of this chapter describes the balanced homodyne detector which we have combined with pump-probe experiments.

Another step towards the goal of studying quantum states in condensed matter

¹The reason for this is that the most common pulsed laser source produce light at this specific wavelength.

is the measurement of the fluctuations in the transient reflectivity in pump-probe experiments. In general, the average of the intensities of many pulses reflected by the sample is taken. However, also the variance of the reflected intensity seems to contain information about the excitation produced in the sample by the pump pulse. For example, the position of the A_{1g} vibrational mode of Bismuth is mapped in its reflectivity. The variance of the reflectivity contains, therefore, statistical information related also to the \hat{q} observable of the underlying mode. In order to measure statistical properties of the reflectivity, we have built a set-up (described in section 6.2) which allows us to measure the intensity of each probe pulse separately. Standard pump-probe set-ups, instead, use devices that average over a set of successive pulses.

In the final section instead, we discuss a secondary possibility introduced by the balanced homodyne detector. As described in chapter 5, such an instrument is based on a Mach-Zehnder interferometer. Pump-probe experiments measure the variations in the *intensity*-reflectivity of the sample, i.e. the variations in the amount of energy reflected by its surface. This is proportional to the square modulus of the electric field of the wave. The interferometer allows us to study also the phase of the electric field of the probe pulses reflected by the sample and therefore detect the excitation-induced phase-shift.

Laser source The laser system which produces the pulses used in our experiments is depicted in figure 6.1. A Nd:YVO₄ Verdi V18 (Coherent) laser pumps a Mira (Coherent) oscillator, in which the active medium is Titanium doped Al_2O_3 (Ti:Sapphire). The oscillator produces pulses at a 80 MHz repetition rate, with a spectrum which is centred on a wavelength of approximately 800 nm and is 30 nm broad. The average output power is approximately 600 mW.

These pulses are then amplified with the *chirped pulse* amplification scheme. They are first of all stretched and then amplified in a regenerative amplifier RegA (Coherent). The output pulses of RegA are compressed and finally sent to the experimental set-up. The final pulsed beam has a 250 kHz repetition rate and an average power of 1.2 W.

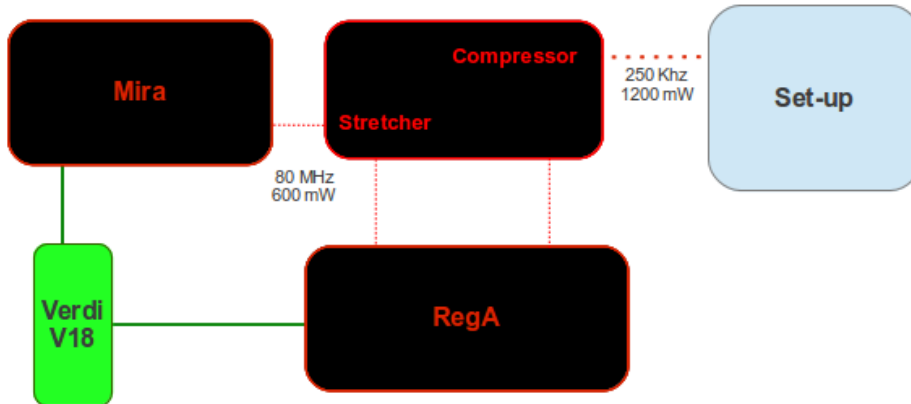


Figure 6.1: Scheme of the laser system

6.1 Balanced homodyne detector for pump-probe measurements

As anticipated, the aim of our balanced homodyne detection set-up is to study the state of the probe pulses after their interaction with the sample. In such a situation, the state preparation of the *signal* occurs in the reflection scattering process of the probe pulses from the sample, which is a Bismuth single crystal in the specific case. As already described, the sample is excited using a second pulsed beam, the pump.

The scheme of our set-up is depicted in figure 6.2. An incoming coherent pulsed beam (produced by the laser source) is split into two by a beam-splitter (BS_1). The reflected beam is used as local oscillator, while the transmitted one as the probe pulse. A different beam coming from the same laser enters the set-up separately from the previous one and is used as the pump. To change the delay between the arrival on the sample of a pump pulse and of the successive probe pulse, the optical path of the pump beam is varied using a mechanical translator (which is placed outside the scheme we are discussing and is not present in figure 6.2). Both the pump and the probe beams are focussed on the sample by the lenses L_p and L_1 respectively and the probe is then collected, re-collimated and sent into the balanced homodyne detector. Before entering the interferometer, however, the beam is filtered by

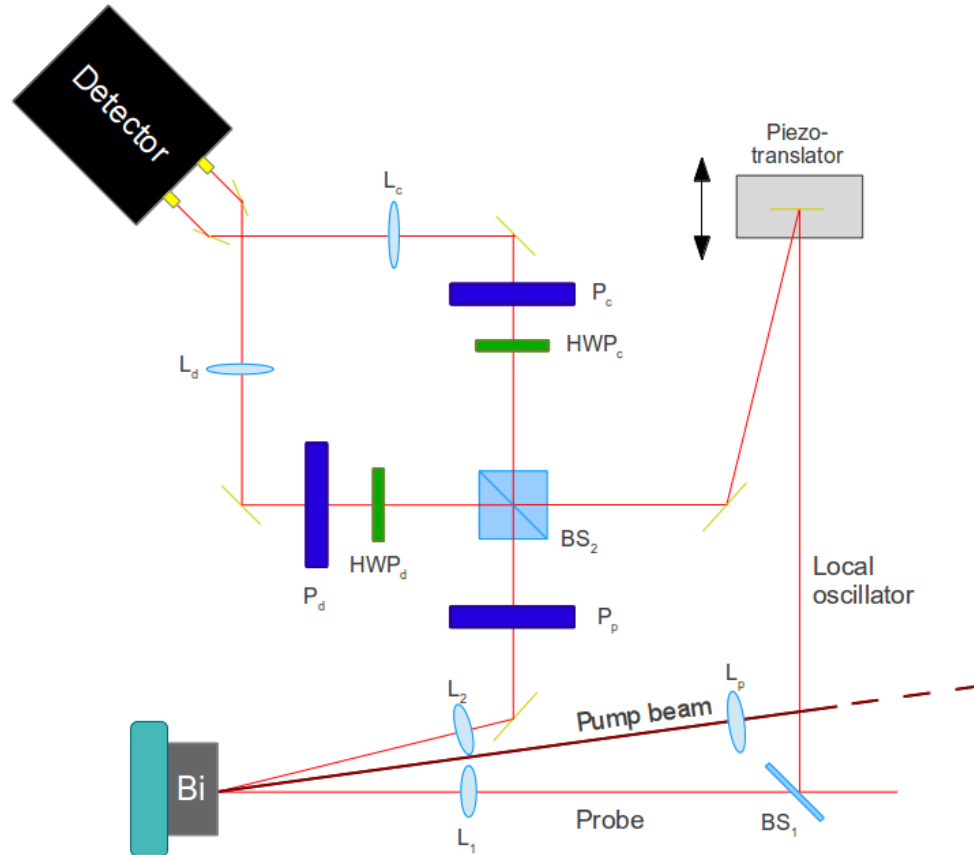


Figure 6.2: Scheme of the balanced homodyne detector adapted to pump-probe experiments

the polarizer P_p . This reduces the scattering from the pump pulses, which are orthogonally polarized with respect to the probe ones, that enters the actual homodyne detector.

On the local oscillator branch, a piezoelectric translator (PI PZ166E) is used to change the phase of the local oscillator. The translator stage has a $250 \mu\text{m}$ total travel range and a 1 nm nominal resolution.

In the upper part of the interferometer, i.e. after the central beam-splitter (BS_2), two couples of half-wave plate and polarizer are used to correct for the

unbalances in the BS_2 itself. Finally, two lenses (L_c and L_d) focus the beams from the two output ports of the central beam-splitter onto the photodiodes.

The acquisition system

The acquisition system used is constituted by a balanced amplified differential photodetector (Thorlabs PDB440A) and a fast digitalizer (Spectrum M3i.2132-exp). The differential photodetector consists of two “well matched” Silicon PIN photodiodes and a low-noise amplifier. The latter outputs a voltage proportional to the difference between the photo-currents produced. As described in chapter 5, the photo-currents are in turn proportional to the number of photons impinging on the photodiodes.

The output voltage of the amplifier, i.e. the difference signal, is measured using a fast 8-bit ADC, which has a maximum sampling rate of 1 GSample/s. This means that we can acquire up to one difference current value every nanosecond. The acquisition board in which the ADC is mounted has an on-board 500 MByte memory, which can be used also as a FIFO-buffer. The board has been bought with a specific option, called *Multiple recording*, which allows to trig the acquisition and to acquire only for a limited time-span each trigger. In fact, the repetition rate of the pulses is 250 kHz, which means that there is a 4 μ s interval between two successive pulses. Since the response of the photodiodes to one pulse lasts for about 40 ns, a continuous acquisition of the output of the amplifier would contain mostly irrelevant data. Instead, by using the *Multiple recording* option and triggering the acquisition with copies of the pulses themselves, the acquisition is limited to the actual “duration” of the pulses, discarding the voids in between, as depicted in figure 6.3.

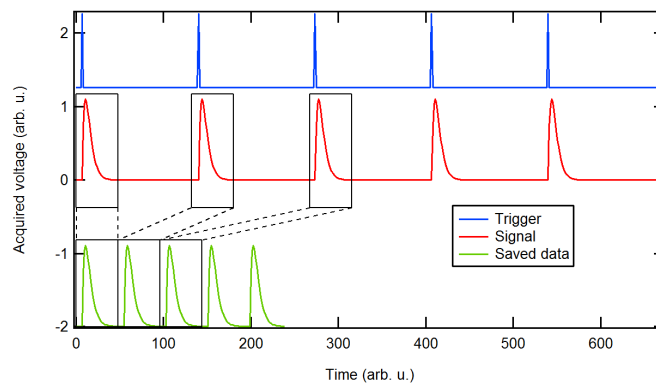


Figure 6.3: Multiple Recording acquisition mode

Characterization of the differential detector

In chapter 5 we have pointed out some of the characteristics of the photo-detection system which are of fundamental importance to balanced homodyne detection. Among them, the shot-to-electronic noise ratio and the linearity of the photodiodes depend on the choice of the experimental working conditions. In fact, there will be an optimal mean power of the beams impinging on the photodiodes. Because of condition 5.7, these intensities are determined by the intensity of the local oscillator, since the signal field must be much weaker. The linear relation between incident intensity and detector's response ensures that what is measured is actually linearly proportional to the photon number. Instead, a high shot-to-electronic noise ratio is needed for the distribution of the difference currents to match the one of the quadratures.

In order to separately characterize the two photodiodes, one of them can be physically covered to stop the beam. In this way, the modulus of the difference signal is the signal produced in the uncovered photodiode. When the intensities of the two beams are equal, the difference trace and the single-diode traces acquired by the digitalizer for each pulse are like the following:^{2,3}

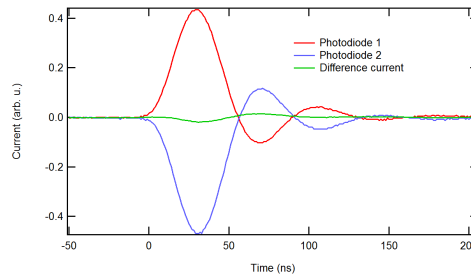


Figure 6.4:

The acquired traces are then integrated and the average is taken from a set of thousands of them. In graphs 6.5 the average integrated current over a set

²Note that the pulse duration is well below the time-resolution of any photodiode. The shape of the trace is then given by the detector's response.

³The difference trace is not exactly zero for all times, as it should because of the equal intensities of the beams. This is due to imperfect subtraction efficiency of the detector. The polarizers and half-wave plates in the upper part of the interferometer can be used to minimise it balancing the two beams. However, since this residual *zero*-response is constant, it can be ignored for all purposes and subtracted in the data analysis procedures.

of 32 000 pulses produced in the two single photodiodes is plotted against the intensity of the beam.

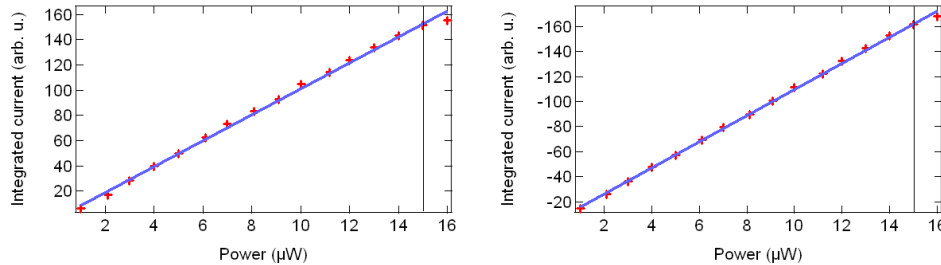


Figure 6.5: Linearity test for the single diodes: integrated current vs beam mean power.

In figure 6.6, we plot of the variance of the difference current as a function of the mean power of the beam.

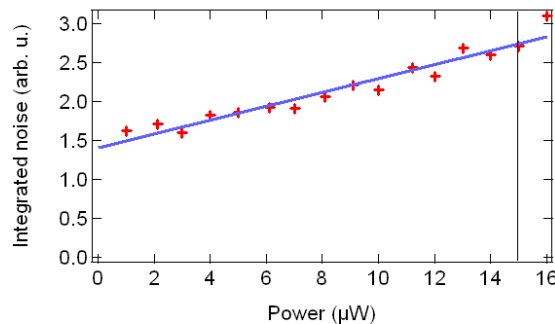


Figure 6.6: Shot noise test: variance of the integrated difference current vs beam mean power.

As one can see from graphs 6.5 and 6.6, 15 μW is the highest local oscillator mean power allowed for balanced homodyne detection. In fact, above 15 μW the intensity-current relation is not linear and the noise ceases to increase linearly with the intensity, i.e. it ceases to be shot-noise limited. The linear-regime interval for the detector is therefore $[0, 15] \mu\text{W}$.

Another relevant fact is that the noise does not go to 0 as the intensity of the impinging beam decreases. This means that there is, a part from shot noise, a constant electronic noise background. The optimal power is the one which maximizes the shot-to-electronic noise ratio and is, hence, 15 μW . For this value of the power, the ratio is 1.86.

High electronic noise condition

Despite the fact that, at $15 \mu\text{W}$ of working mean power, the shot noise is a large contribution to the total noise in the measurement, the shot-to-electronic noise ratio reported for this set-up is too small for the standard Wigner function-reconstruction algorithms. In fact, electronic noise can be described as an equivalent inefficiency of the detector [13] and such a value of the ratio leads to a total equivalent efficiency which is lower than 0.5. The latter is a critical limit for standard reconstruction algorithms. However, this problem can be compensated using specifically adapted algorithms, which require the acquisition of a large amount of data [14].

As an alternative, it is possible to extract partial information on the state measuring electronic noise-free quantities. An example is the correlation between the currents produced in the two photodiodes at a given phase, in the hypothesis of a time-independent electronic noise [15].

6.2 Noise pump-probe measurements

The transient reflectivity changes induced by the excitation in pump-probe measurements are very small. Generally the relative variation of the reflectivity (and hence of the intensity of the reflected probe) is below 10^{-2} . Thus a method to overcome the noise and the fluctuations in the laser source and to resolve such tiny variations is needed.

In the standard pump-probe set-ups this task is addressed by modulating the relevant signal at a specific frequency and filtering the output of the photodiode with a lock-in amplifier. The modulation of the signal is achieved chopping the pump beam, e.g. with a mechanical chopper.

The set-up we have built does not need such a modulation and allows us to acquire large amount of data with a significant statistics in very short times. It is a balanced set-up for pump-probe measurements built with the same differential photo-detector used for the balanced homodyne detector. The scheme of the set-up is depicted in figure 6.7. In figure 6.8, located at end of this section, we show that it is compatible with the balanced homodyne detector, i.e. we can switch between one set-up and the other by simply raising two flip-mirrors.

An incoming pulsed beam is split in two by a beam splitter. The reflected beam, used as a reference, is directly focussed on one of the photodiodes of the detector, while the transmitted one is used as probe. After the interaction with the sample, the latter is collected and focussed on the second photodiode. The reference beam is attenuated in order for its intensity to be equal to the

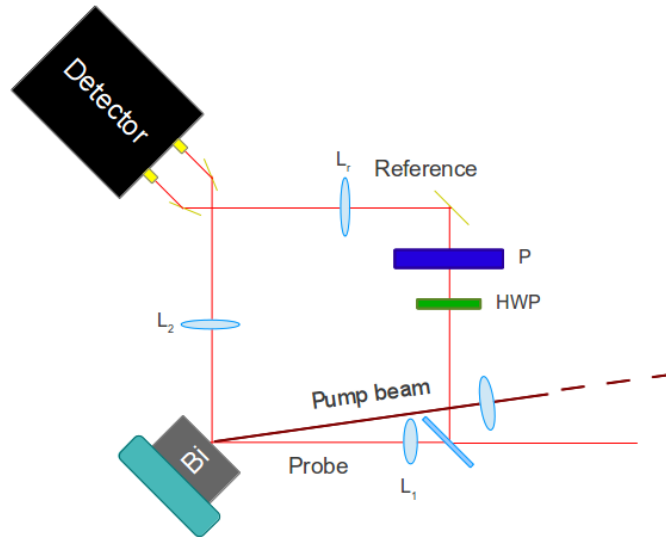


Figure 6.7: Scheme of our balanced set-up for pump-probe measurements

intensity reflected by the sample at equilibrium. This is done by blocking the pump beam (i.e. leaving the sample at equilibrium) and minimizing the output of the differential detector with the help of the half wave plate and the polarizer placed on the path of the reference beam. When the sample is instead excited and its reflectivity is different from the equilibrium one, the intensity of the reflected probe and the one of the reference beam are different. Therefore, the output of the differential detector is proportional to the intensity difference ΔI and hence to the reflectivity variation ΔR of the sample.

The first advantage of a balanced measurement in this context is the intrinsic cancellation of the fluctuations of the laser source without the need of any lock-in amplifier or similar objects. In fact, if the total intensity fluctuates of δ , the differential output is

$$(I + \Delta I)(1 + \delta) - I(1 + \delta) = \Delta I(1 + \delta).$$

Thus, the variations of the reflected intensity due to the sample are not hidden by the total fluctuations, as they would be in the measurement of

$$(I + \Delta I)(1 + \delta).$$

As a second point, since a lock-in amplifier is unnecessary, each pulse can be separately acquired using the fast digitalizer. This allows us to collect large

amount of “statistically significant” data in very short times. In fact, at the repetition rate used, 250 000 pulses are available each second and each of them can be acquired, integrated as described in section 6.1 and its integral stored as a value of ΔR . Generally, we acquire some tens of thousands of pulses for each pump-probe delay. This is done in a fraction of a second. With such a set of data we can calculate the average of the intensity for each pump-probe delay and obtain $\frac{\Delta R}{R}(t)$.⁴ Moreover, we can calculate also the variance of the distribution of $\Delta R(t)$. Previous works [16] already reported noise measurements of the transient reflectivity in pump-probe experiments. These had been performed using a lock-in amplifier and over long times. However, it has been shown [17] that the *integration time* set on the lock-in amplifier has a major role in determining the noise. Moreover, the long acquisition-times expose the measurement to low-frequency noise normally present in an experimental set-up. Successive measurements performed with such a device are therefore statistically unreliable for what concerns moments of the distribution of order higher than one. With our set-up, instead, we can calculate the pulse-to-pulse noise, avoiding artifacts due to devices like a lock-in amplifier and low-frequency noise.⁵

6.3 White light pump-probe measurements

We have also performed broadband pump-probe experiments on Bismuth, i.e. pump-probe measurements in which the probe is a broadband white light pulse instead of a quasi-monochromatic one. In this way, the variations in the reflectivity of the sample can be studied on a wide range of wavelengths, namely from approximately 500 nm up to 800 nm. Compared to what can be known with “monochromatic” pump-probe experiments, a clearer picture of the induced dynamics can be extracted. The set-up we have used for this kind of experiments is not based on a balanced detection system as the one for the pulse to pulse noise measurements. In order to separate the information about the different wavelengths contained in the white light, the white probe pulses are dispersed on a photodiode array by a prism, as sketched in figure 6.9. The measurements performed are reported in chapter 8.

⁴The value of R used to normalize ΔR , is obtained, a part from common proportionality factors, as the average intensity of the reference pulses. The photodiode hit by the probe is covered and some thousands of reference pulses are acquired. The average of the integral of the acquired traces is the value of R .

⁵We have verified that the responses of the detector to successive pulses are uncorrelated.

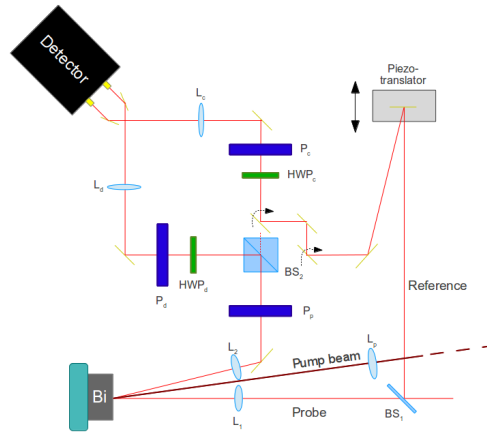


Figure 6.8: The integration of the balanced set-up for pump-probe measurements in our homodyne detector. In this configuration, the piezo-translator is not used. The fact that half of the intensity of the probe pulses is lost on the central beam-splitter is compensated attenuating the reference beam.

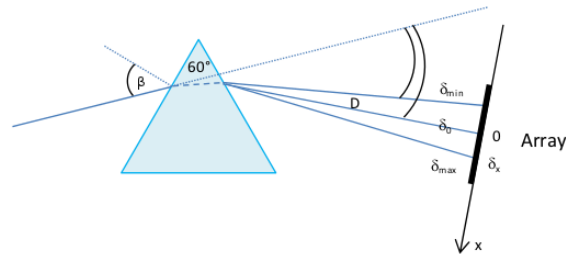


Figure 6.9: A prism is used to disperse the white-light broadband probe onto an array of photodiodes.

6.4 Transient phase-shift measurements

As anticipated in the introduction to this chapter, the interferometer which the homodyne detector is built upon can be used to study the phase of the probe pulses' electric field. To do this, it is not necessary to satisfy condition 5.7 on the intensity of the signal field. We can, hence, work in the classical regime of the interferometer. Considering the signal field in a coherent state $|\alpha\rangle$,

equation 5.5 becomes

$$I_{\Phi} = \sqrt{2}|z||\alpha|\cos(\Phi),$$

where Φ is the phase difference between the signal and the local oscillator. In fact, scanning the values of Φ with the help of the piezo-translator, the set-up can be used to measure the classical linear autocorrelation pattern of the pulse.

When the reflectivity of the sample changes because of the excitation, both the real and imaginary part of the dielectric function change. There will, therefore, be a phase-shift of the reflected electric field with respect to the equilibrium situation. The measurement of the modulus and phase of the reflected field is equivalent to the polarization ellipsometry techniques. To our knowledge, however, such phase sensitive measurements are not usually performed.

In order to measure a phase shift we need to acquire, for each pump-probe delay, the difference current I_{Φ} for at least a significant portion of a cycle of the interferometric pattern. Fitting the sinusoidal curve obtained we can extract a value for the phase, which, however, is still arbitrary. We still need a reference to make a comparison with the phase of the electric field reflected by the sample at equilibrium. The scheme we have adopted is the following: We chop the pump beam using a mechanical chopper, as shown in figure 6.10. In this way, we have time intervals in which the probe is alternatively reflected from the sample at and out of equilibrium. Exploiting the fact that the piezo-translator can be moved in a continuous way, we can make fast scans, that last for about 150 ms, over a portion of the interferometric pattern. Continuously acquiring the values of the difference current during these scans, a pattern is retrieved which is split in various intervals, alternatively referring to the sample at and out of equilibrium. The problem is now to be able to automatically split the interferometric trace in the two sub-traces made of the pumped and unpumped segments. This is possible using the BXIO (basic express input/output) option of the M3i.2132-exp acquisition board. The BXIO option allows to acquire up to 8 digital channels synchronously to the main analog channels of the ADC. Using a beam-splitter to reflect part of the chopped pump beam on a photodiode and connecting the latter to one of the BXIO digital channels⁶, we can associate the status of "pumped" or "at equilibrium" to each difference current value acquired.

⁶The photodiode must be saturated by the pump beam. In this way its output is a square wave which can be used as a digital signal.

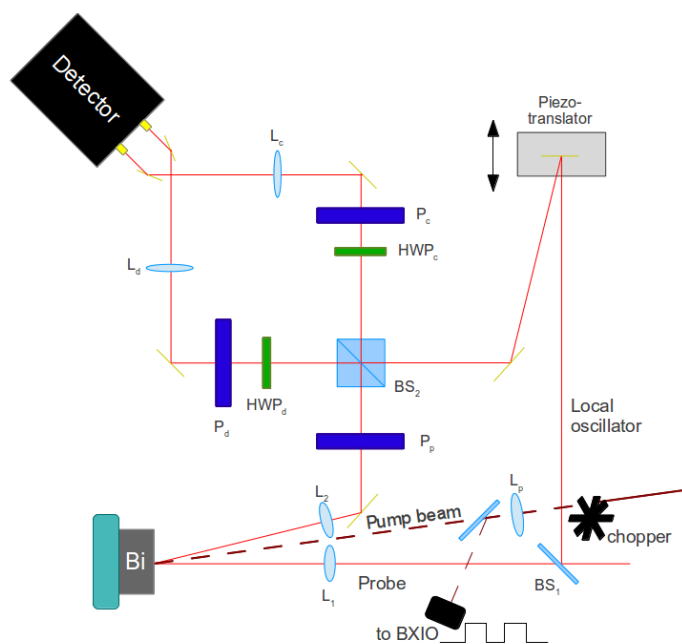


Figure 6.10: Our set-up for the measurement of transient phase-shifts in pump-probe experiments

In appendix D we discuss an alternative way of measuring the transient phase-shift.

Chapter 7

Bismuth

Most of the elemental metallic crystals are either cubic (body- or face-centred) or hexagonal close-packed. Exceptions to this are Arsenic, Antimony and Bismuth, whose structure is called α -Arsenic (or A7) [18]. In particular, this structure can be described as a distorted simple cubic one, in which the atoms have dimerized along the [111] direction. This means that the inter-atomic distances have alternating values on the mentioned axis. The one-atom elementary cell of the ideal simple cubic crystal therefore becomes a two-atoms cell in a face-centred cubic lattice.

The departure from the simple cubic structure arises from the fact that the distortion and the related symmetry reduction are favoured by a gain in electronic energy, as described in the following section. Therefore, there is a strong coupling of electronic degrees of freedom and lattice vibrations along the [111] direction. This coupling, in turn, lies at the core of the “coherent” vibrational response which is observed in pump-probe experiments on these systems. This will be described in more detail in section 7.3. This phenomenon is the reason that triggered us to take Bismuth as model system for this project. In fact, the most intuitive condensed matter equivalents to photonic states are phononic ones, which had been extensively studied in this system from a classical point of view.

7.1 Jones - Peierls distortion

In trying to understand the structure of crystals, it is natural to think of forces between the constituent atoms [19]. Considering that these depend on the distances between atoms and that bonds can be directional, one can account for the structure of the majority of crystals. However, the structure of elemental

Bismuth and of the other A7 elemental crystals cannot be explained with such arguments. As already anticipated, it is a slightly distorted simple cubic lattice in which one atom every two has moved along the diagonal of the cube¹. Therefore, the symmetry of the actual structure is lower than that of the ideal one. The distorted structure displays unit cells which contain two atoms and which form a face-centred cubic lattice. Its first Brillouin zone is inscribed in the cube of edge $\frac{2\pi}{a}$, corresponding to the undistorted case, as depicted in figure 7.1.

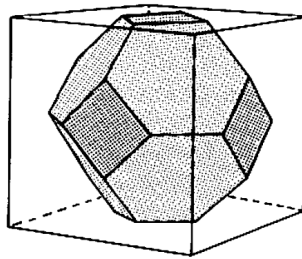


Figure 7.1: First Brillouin zones of a face-centred cubic and of a simple cubic lattice.

The number of states (spin and orbital) for an electronic band within the new zone is twice the number of unit cells (i.e. one for each atom) and Bismuth atoms have an odd number of electrons (83). Thus, most of the states inside the new zone are filled, while most of the ones outside are empty. The surfaces of the new zone which lie within the volume of the ideal one act to open a gap, lowering the energy of the states within the Brillouin zone, which are mostly filled, and raising the energy of the ones outside, which in turn are mostly empty [20]. Thus, breaking the symmetry brings to a net lowering of the total electron energy. This is called Jones-Peierls distortion. On the other hand, the interaction between the atomic cores tends to favour the symmetric configuration. The stable low-symmetry configuration is justified by a dominating electronic energy gain.² Figure 7.2 shows the opening of the Peierls gap in the one-dimensional case, while figure 7.1 shows the three-dimensional case with a simplified Fermi surface.

However, despite the opening of the gap, Bismuth is a conducting material, albeit a poor one (a semi-metal). In fact, as already mentioned, neither the

¹There is also a slight misalignment between the ideal cube diagonal and the dimer axis in the distorted lattice. However, this further detail does not affect the argument presented.

²The one-dimensional equivalent of this process is known as Peierls distortion [19].

states inside the Brillouin zone are all filled nor the ones outside are all empty, and therefore both electrons and holes conduction still takes place.

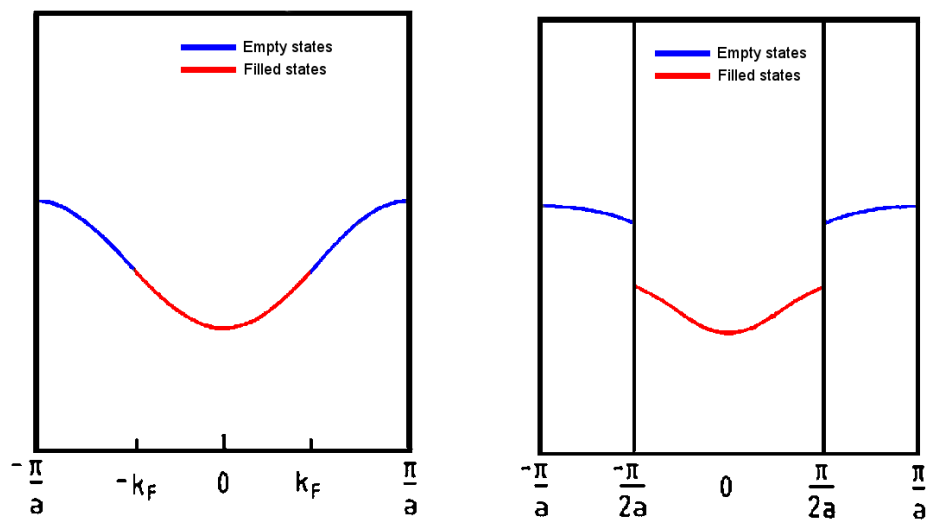
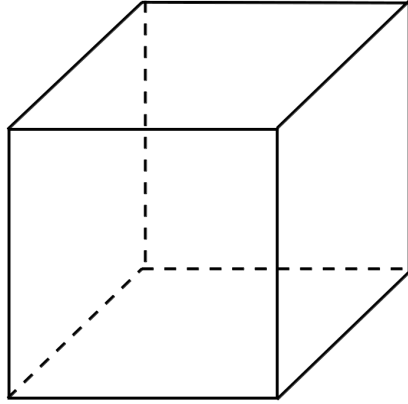
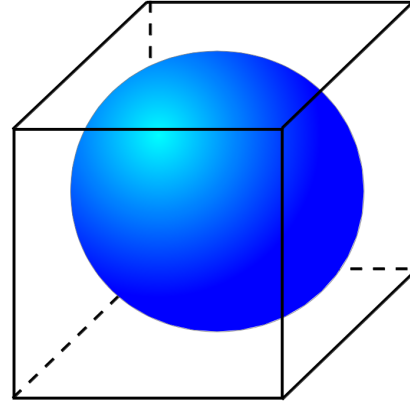


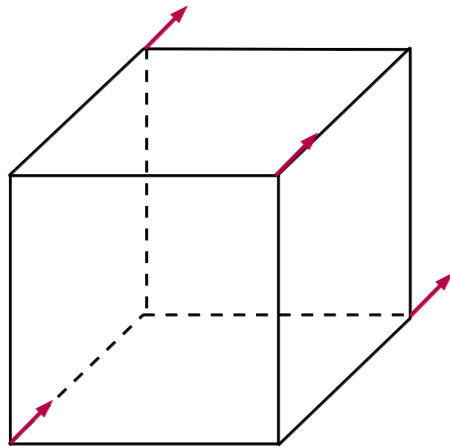
Figure 7.2: One-dimensional case of the Peierls distortion.



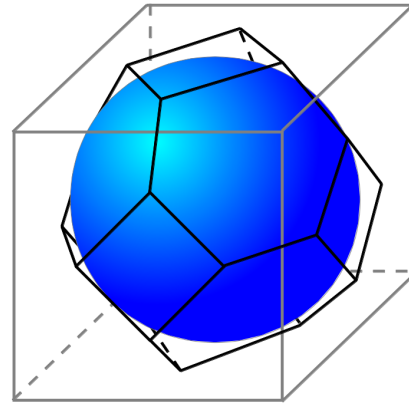
Real space ideal simple cubic lattice.



First Brillouin zone of the ideal simple cubic lattice and a simplified Fermi surface.



Real space distorted face-centred cubic lattice.



First Brillouin zone of the distorted structure and a simplified Fermi surface.

As we will discuss later in more detail, the Jones-Peierls distortion straightforwardly couples the atomic positions along the $[111]$ axis to the electronic degrees of freedom. This is of fundamental relevance to the kind of pump-probe experiments we will discuss in this thesis.

7.2 Unit cell and active phonons

In this section we will analyse which symmetries are allowed for the lattice vibrations in such a crystal. The A7 α -Arsenic structure has the symmetry of the $R\bar{3}m$ space group and its unit cells interact with the surrounding environment in a D_{3d} -symmetry. The D_{3d} point group contains the identity E , two C_3 rotations of $\frac{2}{3}\pi$ around the z-axis (which in this case is the dimer axis), three C_2 rotations of π around axes orthogonal to the dimer-axis, the inversion i , two roto-reflections S_6 around the z-axis and the mirror reflections σ_d about three planes containing the two atoms of the unit cell. The full character table of the irreducible representations for the D_{3d} group with their linear and quadratic bases is reported in appendix C.

The characters of the representation Γ of the atomic coordinates are the following,

$$\begin{array}{c|cccccc} & E & 2C_3 & 3C_2 & i & 2S_6 & 3\sigma_d \\ \hline \Gamma & 6 & 0 & 0 & 0 & 0 & 2 \end{array}.$$

These characters are the traces of the matrices representing the operators of the group in the base of the cell's atom coordinates. The decomposition of Γ in the irreducible representations of the group is reported in table 7.1. Therefore, Γ can be written as

$$A_{1g} \oplus E_g \oplus A_{2u} \oplus E_u.$$

From the character table in appendix C, the A_{2u} and E_u representations correspond to objects that behave like polar vectors and therefore to the acoustic vibrational modes of the lattice. They are the frustrated translations of the unit cell blocked within the crystal. The remaining two representations, A_{1g} and E_g , correspond to optical modes. The E_g mode is the frustrated rotation of the cell around an axis orthogonal to the dimer-axis. The A_{1g} one is, instead, the fully symmetric one and is the axial vibration of the two atoms in the unit cell.

Neither of the two optical modes can be excited via an electric-dipole transition with an initial fully symmetric state. In fact, depending on the radiation-crystal geometry, the irreducible representations for the dipole operator is the E_u or the A_{2u} and none of the optical modes has one of these symmetries. They are instead both Raman-active.

In order to preserve the symmetry of the unit cell, the atomic displacements in the A_{1g} optical mode must be along the z-axis. The latter corresponds to

	$1E$	$2C_3$	$3C_2$	$1i$	$2S_6$	$3\sigma_d$	
Γ	6	0	0	0	0	2	
A_{1g}	1	1	1	1	1	1	
	$(1 \cdot 6) \cdot 1$	$(1 \cdot 0) \cdot 2$	$(1 \cdot 0) \cdot 3$	$(1 \cdot 0) \cdot 1$	$(1 \cdot 0) \cdot 2$	$(1 \cdot 2) \cdot 3$	$= 1 \cdot 12$
A_{2g}	1	1	-1	1	1	-1	
	6	0	0	0	0	-6	$= 0$
E_g	2	-1	0	2	-1	0	
	12	0	0	0	0	0	$= 1 \cdot 12$
A_{1u}	1	1	1	-1	-1	-1	
	6	0	0	0	0	-6	$= 0$
A_{2u}	1	1	-1	-1	-1	1	
	6	0	0	0	0	6	$= 1 \cdot 12$
E_u	2	-1	0	-2	1	0	
	12	0	0	0	0	0	$= 1 \cdot 12$

Table 7.1: Decomposition of the representation Γ of the coordinates in irreducible representations.

the Jones-Peierls distortion direction of the crystal. The A_{1g} mode is therefore coupled to the electronic degrees of freedom via the distortion mechanism described in the previous section. In fact, a non-zero amplitude in the A_{1g} mode leads to a modulation of the electronic energy gap. Conversely, the excitation of electrons from the “valence” band into the “conduction” band reduces the total energy gain since states become filled which had been raised in energy by the opening of the gap. It therefore destabilizes the distortion and transfers energy into the A_{1g} mode. This excitation process falls under the name of *displacive excitation* [21], since it corresponds to a sudden translation of the equilibrium position for the atomic displacements.

7.3 “Coherent phonons”

The main background phenomenon which this project is based upon is the “coherent”³ vibrational response observed in pump-probe experiments on Bismuth.

The most simple response which can be expected in such an experiment is the production, due to the interaction with the pump pulse, of an excitation and its subsequent thermal relaxation. In such a situation, the reflectivity of the sample behaves in the way depicted in figure 7.3, in which the relative variation of the reflectivity $\frac{\Delta R}{R}$ is plotted as a function of time t (i.e. time-delay between the excitation and the probing, or pump-probe delay).

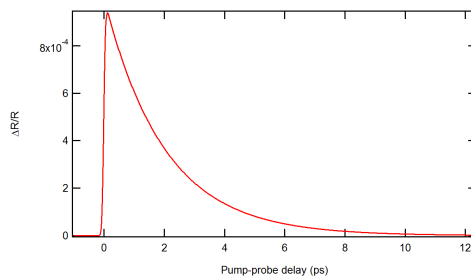


Figure 7.3: Simple pump-probe trace

However, more complex responses can occur (as is the case for Bismuth). As an example, a coherent modulation of the underlying thermal relaxation-signal can be present. In these cases two distinct contributions to $\frac{\Delta R}{R}(t)$ can be identified, which we call coherent and incoherent part, as depicted in figure 7.4. If the frequency of the coherent modulation of the reflectivity corresponds to the known frequency of a vibrational mode in the solid, which can be measured in a scattering experiment (e.g. Raman), the modulation itself can be associated with the presence of a coherent lattice vibration⁴. In these cases, there exists a mechanism which maps the vibrational response, and in particular the vibrational mode’s position (i.e. atomic positions), onto the high-energy optical properties of the sample. In fact, while the energy of vibrational excitations in condensed matter is of tens of millielectronvolts, their presence is mapped, for example, in the reflectivity at ~ 1.5 eV (800 nm). Furthermore,

³In this chapter we will use the term *coherence* in relation to oscillations with a well determined phase. From now on we will drop the quotes here.

⁴Note that there is not necessarily a strict correspondence with quantum coherent states of the vibrational mode considered.

the damping of the coherent part of $\frac{\Delta R}{R}$ is due to the damping of the vibrational oscillation. This is, in turn, caused by the interactions of the phonons with various degrees of freedom.

Bismuth crystals behave as described above. However, Bismuth (as also Antimony) displays coherent reflectivity oscillations whose amplitude is unusually large. As described in the previous section, the A7-structure allows for two different symmetries of optical vibrations. Oscillations at the frequency of the A_{1g} mode can be seen in the transient reflectivity under general experimental conditions. Modulations due to the E_g mode, instead, have been seen in the anisotropic reflectivity change of polycrystalline films [22] or in the reflectivity change of single crystals below 200 K [23].

The efficient mapping and the consequent large contribution of the A_{1g} oscillations to the $\frac{\Delta R}{R}(t)$ signal are due to the coupling of the electronic degrees of freedom and the A_{1g} mode. In order to concentrate on the simplest case, our discussion here will relate to the situation in which only the A_{1g} mode is visible. The measurements which we present in chapter 8 are performed under these conditions too.

One of the parameters which can be varied in a pump-probe experiment is the amount of energy brought by each pump pulse on the sample. However, since the dimensions of the transverse section of the pulse depend on the specific experimental set-up, rather than the energy per pulse, the relevant number is the energy surface density brought by a pump pulse on the sample, which is called fluence and is generally expressed in J/cm^2 .

It has been extensively reported [24, 25, 26] that the frequency of the oscillation changes during the oscillation itself and that, the higher the fluence of the pump pulses, the larger the total frequency shift is. In particular, for short times after the excitation, when the amplitude of the oscillation is large, the phonon-mode is softened, i.e. there is a shift of the frequency towards lower values, whereas it tends to the Raman-measured A_{1g} mode frequency with increasing time.

This effect had been originally ascribed to the anharmonicity of the lattice potential [24]. In fact, the frequency shifts away from the "harmonic" value when the amplitude of the oscillation is large, i.e. when the mode is heavily populated, while it recovers the "harmonic" value when the amplitude becomes small. In classical terms, the larger the amplitude of the oscillation the more the atoms "explore" anharmonic regions of the lattice potential. However, further works have suggested another explanation for the phonon softening, which involves an electronic screening of the lattice potential [27, 18, 28].

Together with the phonon-softening, the oscillation is also damped more strongly

the higher the excitation-fluence is.

It is also known that there is a temperature-dependent equilibrium phonon softening, i.e. the equilibrium frequency of the vibrational mode becomes lower at higher temperatures of the crystal.

Both the thermal equilibrium softening and the dynamical short times softening can be accounted for in the electronic screening picture. In fact, the shape of the potential will depend on the total energy gain. This, in turn, depends on the density of electrons in the conduction band, since the presence of electrons excited across the gap lowers the gain in electronic energy. We can therefore consider the expansion of the mode’s frequency in powers of the electronic density in the conduction band [18, 28]:

$$\Omega(n) = \Omega(0) - a n. \tag{7.1}$$

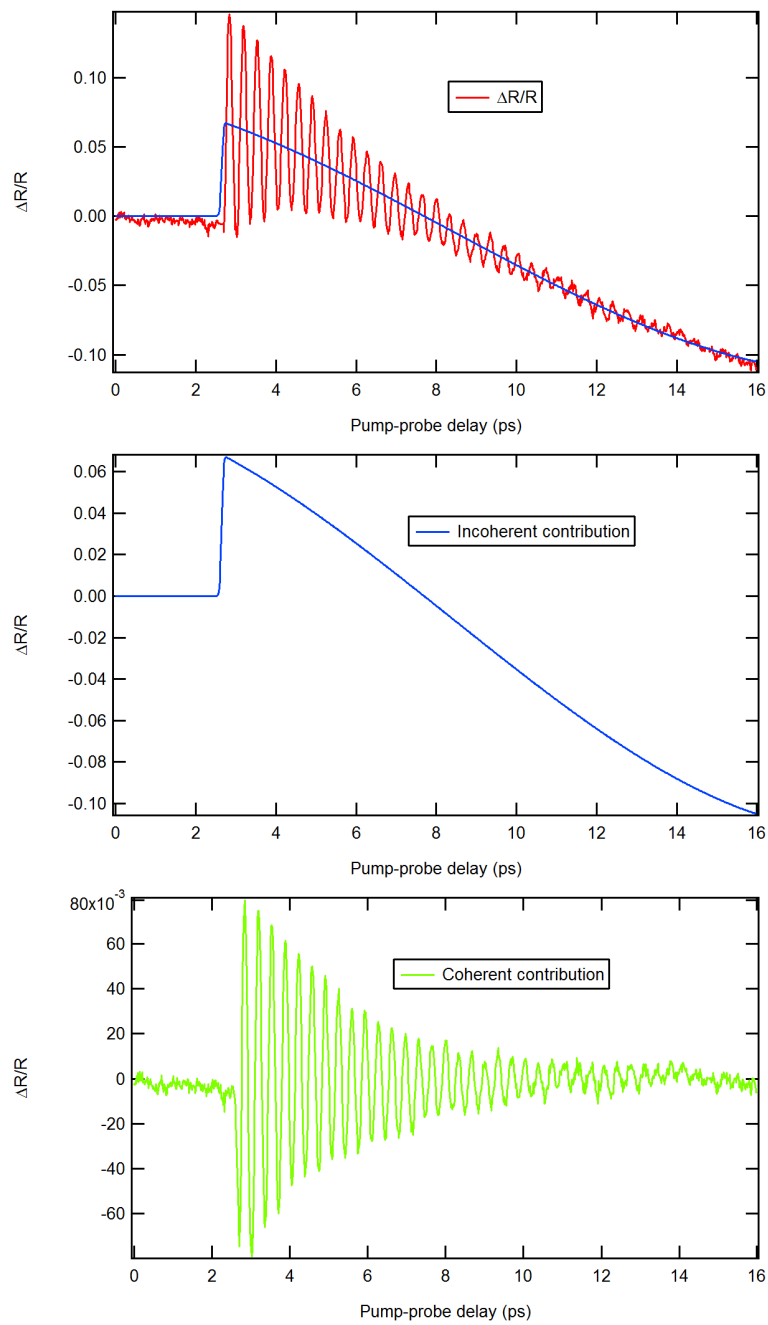


Figure 7.4: $\frac{\Delta R}{R}(t)$ and its incoherent and coherent parts.

Chapter 8

Results

In this chapter we present the analysed data obtained in our pump-probe experiments on Bismuth. The measurements reported in the first section are the reflectivity-noise data, in which we study the behaviour of $\frac{\Delta R}{R}(t)$ and of its variance. As described in chapter 7, the A_{1g} vibrational response of the Bismuth crystal to the excitation is mapped in its high energy-reflectivity. The goal of these measurements is to extract statistical information about the state of the A_{1g} mode through the study of the statistical properties of the reflectivity. These are the first step in the core direction of the project. In fact, also the full tomography of a state consists of the measurement of its statistical properties. The measurements we report here, however, do not constitute a tomographic reconstruction, because the vibrational mode evolves in time due to interactions, and the statistical information about its state is only partial for every pump-probe delay. Moreover, the observed statistics is not necessarily exclusively related to the vibrational dynamics but can contain contributions due to the transient dynamics of the electrons. The mapping process could map the statistics of the underlying vibrational state in a non-faithful way.

The other two sections contain data, which are auxiliary to the project. They do not play a role in the determination of the state of the system but are helpful to have a clearer picture of the phenomenon occurring in the sample out of equilibrium. In particular, they could help to understand in more depth the mapping process of the vibrational response into the high-energy optical properties. Pump-probe measurements with white light-probes (section 8.2) are useful to track the variations of the reflectivity over a broad energy-interval. The measurement of the transient phase-shift in the field and hence, in the field-reflectivity r , (section 8.3) is, instead, an alternative to time-resolved

polarization ellipsometry.

8.1 Noise in “monochromatic” pump-probe measurements

The set-up we use to perform pump-probe noise measurements is described in detail in section 6.2. The key feature is that we can acquire a large set of $\frac{\Delta R_i}{R}(t)$ values at each pump-probe delay t . Taking their average

$$\frac{\Delta R}{R}(t) = \frac{1}{N} \sum_i \frac{\Delta R_i}{R}(t)$$

(separately for each delay) we obtain the standard pump-probe trace, e.g. the one in figure 8.1. Moreover, with such a large amount of data, it is also possi-

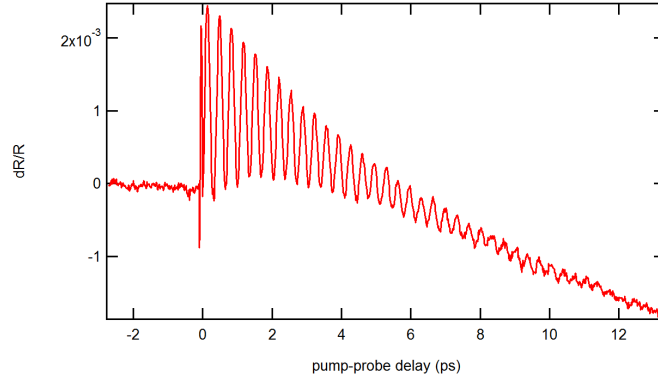


Figure 8.1: A standard reflectivity pump-probe trace: $\frac{\Delta R}{R}$ is plotted as a function of time (i.e. pump-probe delay). Note that the spike at 0 pump-probe delay is due to the interference between the pump and the probe pulses.

ble to reliably calculate the variance of $\frac{\Delta R}{R}(t)$ for each pump-probe delay. As mentioned in chapter 6, the acquisition of, say, 50 000 values of $\frac{\Delta R}{R}(t)$ takes 0.2 s, which is below the low-frequency noise characteristic times that can be relevant in a laboratory. Moreover, thanks to the fast digitalizer and to the balanced detector, we perform single pulse measurements, which are free from possible distortions induced by intermediate instruments and which we have verified to be uncorrelated one with another. The acquisition of the reported data was done in the following way: For each pump-probe delay we acquired 50 000 values for $\frac{\Delta R_i}{R}(t)$, which were used to calculate the average and the

variance values. We repeated the pump-probe delay scan many times (from 10 up to 100 times, depending on the set of data). The plotted data, for both the reflectivity and its variance, are the average over these scans. A variance calculated in this way has no statistical significance over the full set of data for each pump-probe delay (50 000 points \cdot the number of scans) but such a procedure allows us to retain only the features in the variance signal that appear in all the scans.

As described in chapter 7, it is well known that the higher the excitation fluence the stronger the damping of the coherent oscillation, i.e. the smaller τ is. We performed measurements with different excitation-fluences in slightly different experimental conditions, i.e. different points on the sample and slightly different pump spot size. In order to have the labelling of the measurements as uniform as possible, we preferred to associate them with the oscillation’s damping time τ rather than with the pump fluence. The time τ was extracted, together with other parameters, with a fit of the coherent part of the transient reflectivity signal (see section 7.3). The first step was to subtract the incoherent contribution of the signal. In order to avoid complications of the fitting functions which would have been useless in this specific context, we considered only the data for pump-probe delay $t \geq 0$. A fit with a low-order polynomial gives the incoherent part of the signal, since such a function is unable to follow the high-frequency oscillations of the reflectivity signal.

Once the incoherent contribution has been extracted, the coherent one is the difference between the signal and the fitted polynomial. These data can be then fitted with an oscillating function. The latter takes into account, apart from the damping, also the frequency variation due to the “phonon”-softening¹, and is

$$f(t) = f_0 + A \sin(2\pi\nu(1 - b e^{-t/c})t + \phi) e^{-t/\tau}. \quad (8.1)$$

In the above expression, A is the initial oscillation’s amplitude, ν is the asymptotic oscillation frequency while b is the fraction of which ν is softened. c is the decay time of the softening and ϕ is the oscillations initial phase. Finally, τ is the damping time, which is used here as a label for the different set of data. The exponential function for the frequency can be justified considering the linear dependence between the frequency and the electron density in the conduction band (already mentioned in chapter 7) [18, 28],

$$\nu(n) = \nu^{(0)} - a n. \quad (8.2)$$

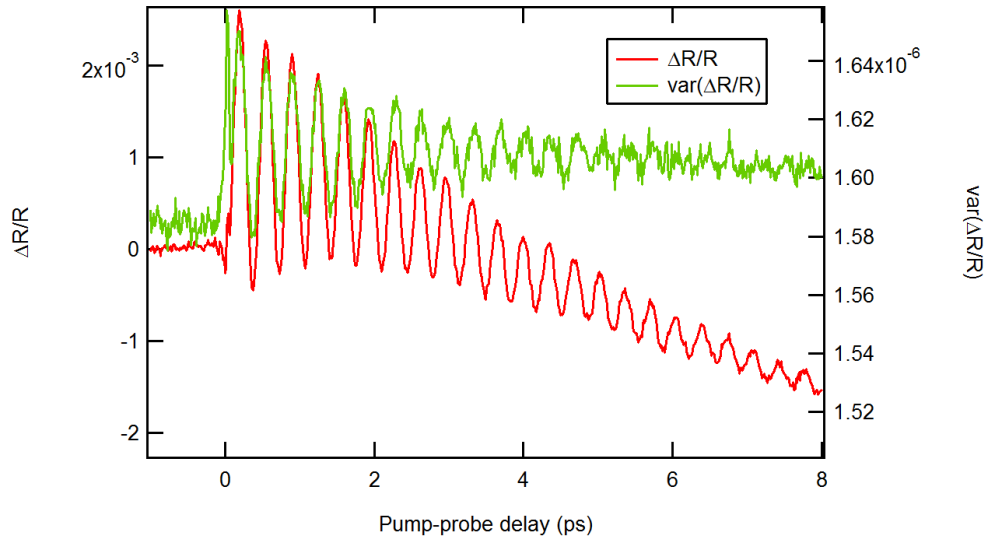
¹Described in section 7.3

The used fitting function can be retrieved supposing an exponential decay of $n(t)$ after the excitation:

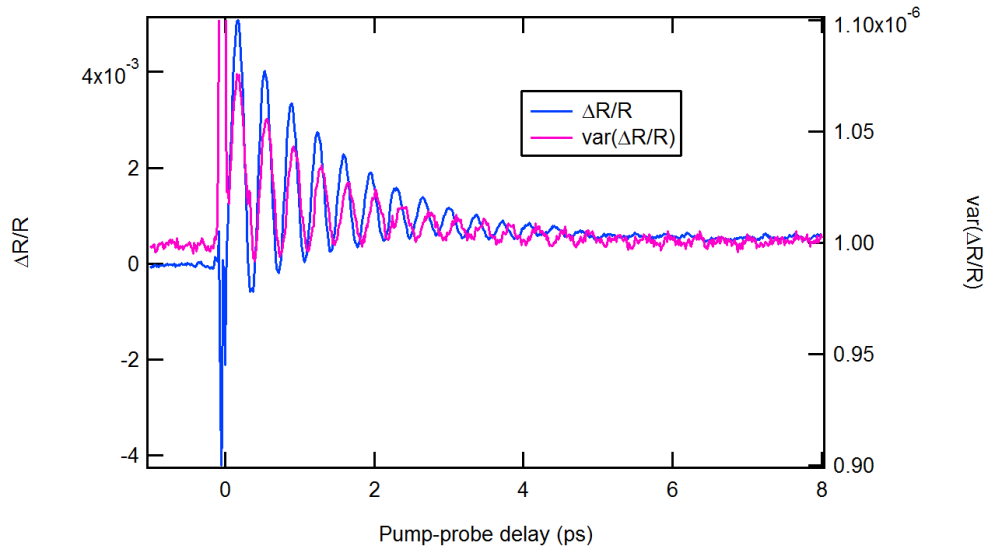
$$\begin{aligned}\nu(t) &= \nu^{(0)} - a n_0 e^{-t/c} \\ &= \nu^{(0)} \left(1 - \frac{a n_0}{\nu^{(0)}} e^{-t/c} \right).\end{aligned}\tag{8.3}$$

The acquired noise data shows that for $t \geq 0$ also the variance displays a periodic modulation as a function of time. For weak dampings, the $\frac{\Delta R}{R}(t)$ -variance's oscillation seems to follow the $\frac{\Delta R}{R}(t)$ signal, i.e. the two frequencies are the same within experimental errors. For strong dampings instead, there is a significant mismatch between the frequencies at which the average and the variance oscillate. For this reason, we adopted the same fitting procedure described in the previous passages also for the $\text{var} \left(\frac{\Delta R}{R} \right)(t)$ signal. We report two of the most representative sets of data, the one for $\tau = 2.89$ ps and the one for $\tau = 1.21$ ps. Figure 8.2 reports the plots of the reflectivity and of its variance in the two cases. Figure 8.3 reports instead the time-dependent frequencies for the four traces as obtained by the fit, and hence

$$\nu(t) = \nu(1 - b e^{-t/c}).$$



$\frac{\Delta R}{R}(t)$ and its variance for $\tau = 2.89$ ps.



$\frac{\Delta R}{R}(t)$ and its variance for $\tau = 1.21$ ps.

Figure 8.2:

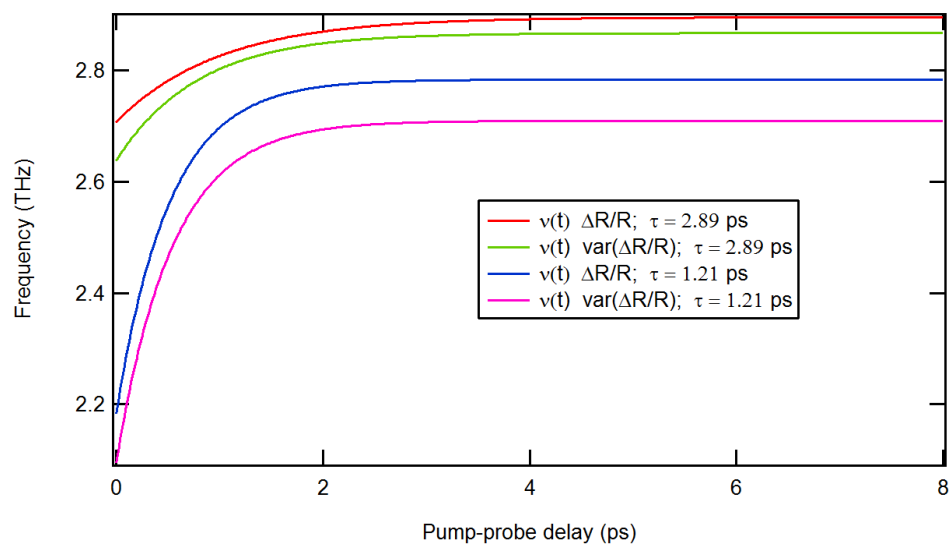


Figure 8.3: Frequency of $\frac{\Delta R}{R}$ and of its variance as a function of t for $\tau = 2.89$ ps and 1.21 ps.

As shown in figure 8.4 and as previously reported in other works [24, 25, 26], the short times-frequency of $\frac{\Delta R}{R}(t)$ (calculated as $\nu_0 = \nu(1 - b)$) is lower for stronger damping, i.e. small τ and high fluence. We could not go to smaller τ s because higher fluences would damage the sample.

Looking at figure 8.5, it is clear that the asymptotic frequency is not constant with τ . This general softening of the vibrational mode, which does not depend on the oscillation’s amplitude, can be ascribed to the pump-induced heating. In fact, previous works [18] reported a dependence of the frequency of the A_{1g} mode as a function of the temperature of $0.012 \text{ cm}^{-1}/\text{K}$.

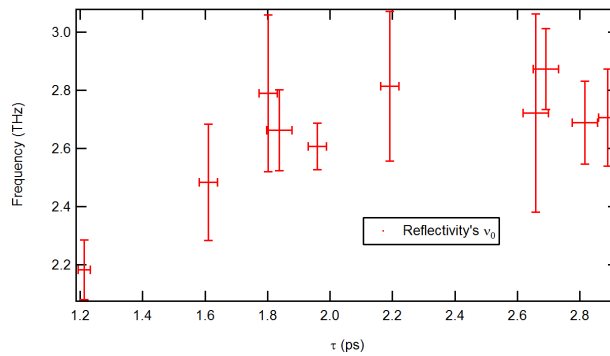


Figure 8.4: Initial frequency ν_0 of the reflectivity’s oscillation vs damping time τ .

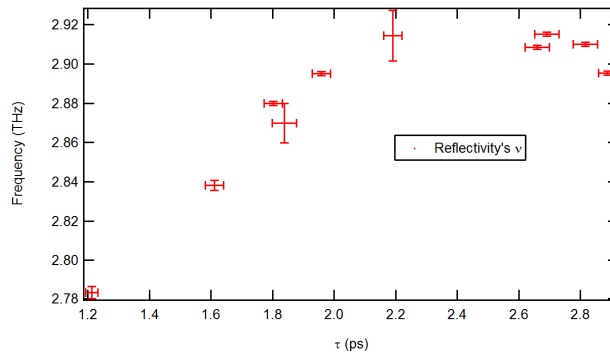


Figure 8.5: Asymptotic frequency ν of the reflectivity’s oscillation vs damping time τ .

For what concerns the variance $\text{var}\left(\frac{\Delta R}{R}\right)(t)$ we report the same kind of graphs, in which we plot ν and ν_0 of the variance as a function of the *reflectivity's* damping time τ . In figure 8.6 we do not report the error bars, because, given the quality of the variance signal, the errors provided by the fitting procedure on the parameter b (and hence of ν_0) are very large for many of the points. They would hide the underlying trend. However, it must be remarked that the $\nu_0(\tau)$ plot could be non-significant.

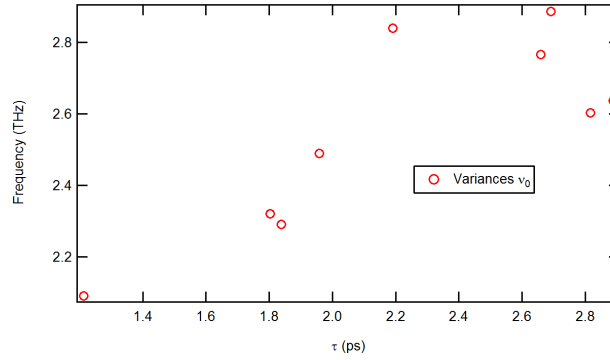


Figure 8.6: Initial frequency ν_0 of the variance's oscillation vs the *reflectivity's* damping time τ . We have excluded the point at $\tau = 1.61$ ps, which is instead present in the plots for the reflectivity, since the relative variance signal is very noisy.

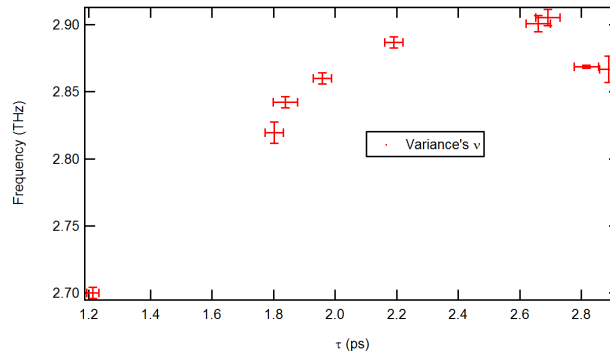


Figure 8.7: Asymptotic frequency ν of the variance's oscillation vs the *reflectivity's* damping time τ .

8.2 White light-probe measurements

As described in section 6.3, we also performed pump-probe experiments with white light-probes. After the excitation of the sample with a quasi-monochromatic pump pulse, a white light-probe is used to study how its optical properties vary in time. Once reflected by the sample, the white light is dispersed by a prism on an array of photodiodes and its spectral content can be studied at different wavelengths.

We report here measurements corresponding to increasing excitation fluences. Each line in the top color maps in figures 8.8 and 8.9 is a $\frac{\Delta R}{R}(t)$ pump-probe trace similar to the ones in the previous section. However, they correspond, here, to the probe energies contained in the interval [1.5, 2.5] eV (while in section 8.1 the reflectivity was measured only at 1.5 eV).

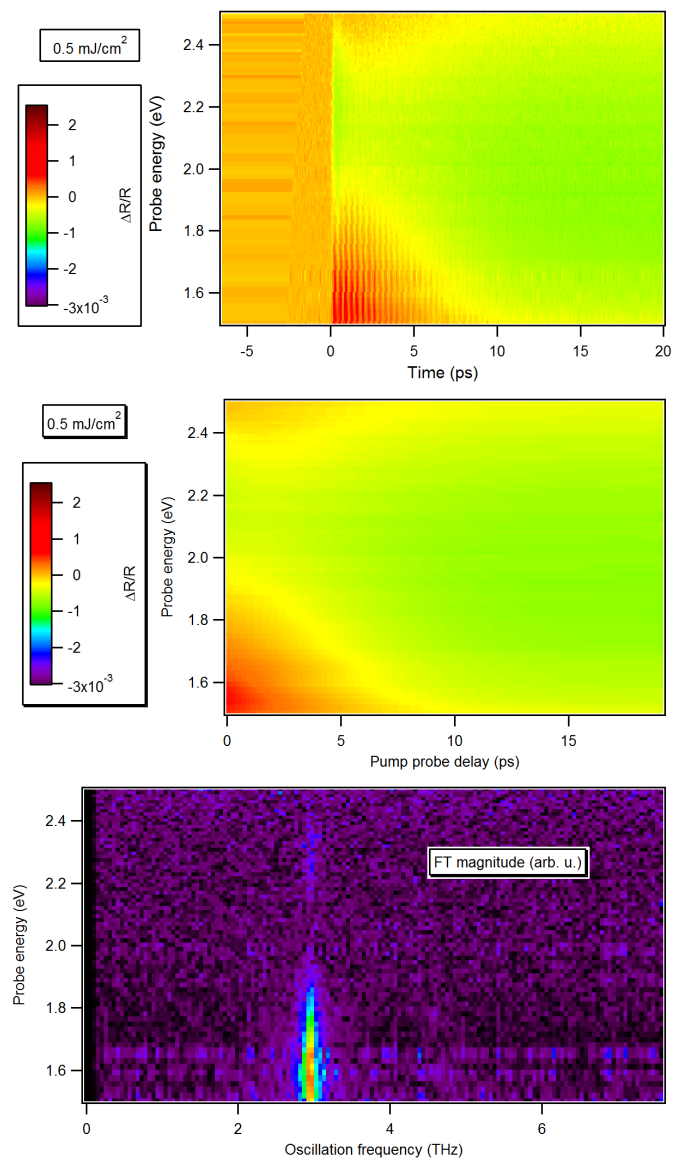
Over this interval, the coherent and incoherent contributions to $\frac{\Delta R}{R}(t)$ are different. In order to extract them, each line of the top color maps² was first of all fitted (from 0 pump-probe delay on) with a low-order polynomial, as previously described. These fits are the incoherent contributions to $\frac{\Delta R}{R}(t)$, and are reported in the second color map of the figures. The oscillating part of the data is extracted as the difference between the data and the fitted function. Calculating the magnitude of its Fourier-transform for each probe energy, we obtained the third color maps. These show the magnitude of the Fourier-transform as a function of both the oscillation frequency in time and the probe energy. The identified frequency is the known one, i.e. approximately 2.95 THz³. However, the amplitude of the reflectivity’s coherent oscillation is not uniform throughout the probed energy interval. This is shown in figure 8.10, which is a vertical profile of the Fourier-transform maps at 2.95 THz. The amplitude of the coherent part of $\frac{\Delta R}{R}(t)$ is large in the interval [1.5, 1.8] eV at all fluences, while it becomes appreciable also between 2.2 and 2.4 eV

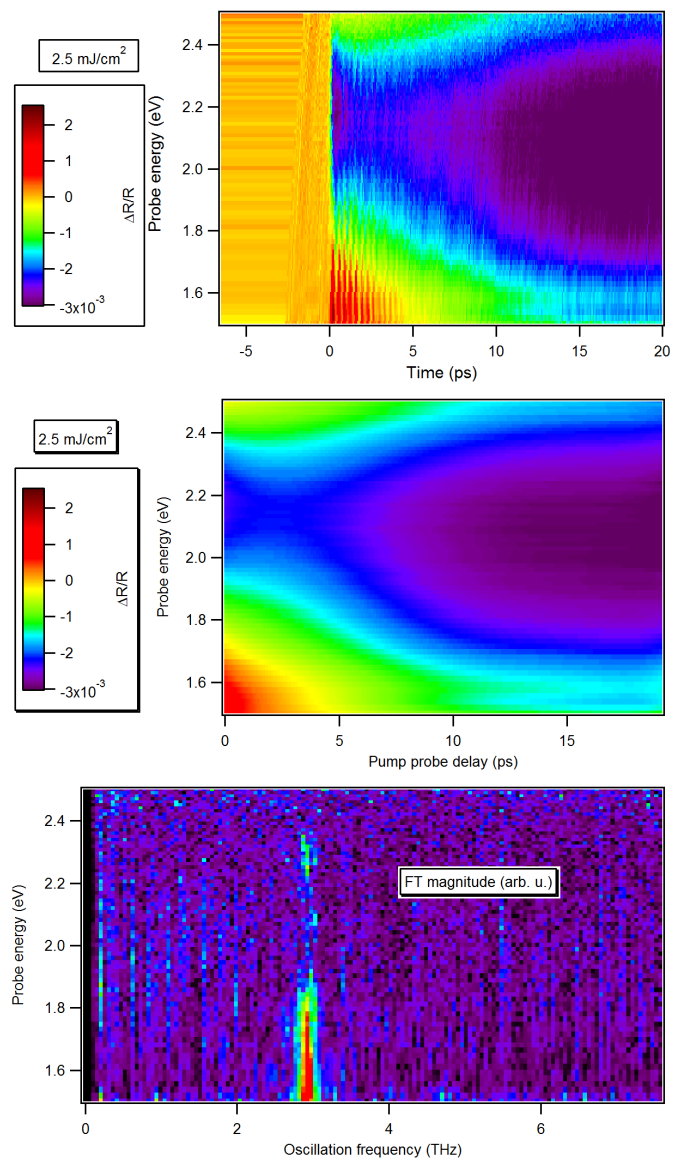
²The white-light pulses are *chirped*, which means that the frequency content of the pulse depends on the temporal position within the pulse itself. In other words, different frequencies arrive at different times. In particular, the chirp is linear and the temporal offsets that have to be applied to the pump probe traces to be re-aligned are a linear function of time. We did not discuss this step in this chapter, since it is mainly technical manipulation of the data. For a discussion about it, see [29].

³The set-ups used for the white light probe experiments and the “monochromatic” ones use two different models of translator to change the optical path of the pump-pulses (and, hence, the pump-probe delay). The mismatch between this frequency and the one measured in the “monochromatic” experiments reported in the previous section ($\nu = 2.92$ THz) can be accounted for by tiny (1/100) miscalibrations of the translators or simply because of the resolution in the fast Fourier transform calculations.

with high excitation-fluences. The electronic degrees of freedom responsible for the reflectivity in these two intervals are therefore coupled to the A_{1g} vibrational mode. Papalazarou et al. [30] report the observation, in time- and angle-resolved photoemission from the (111) surface of a Bismuth crystal, of an electronic band oscillating at the A_{1g} frequency. The amplitude of the oscillation depends on the crystal momentum of the electrons and is larger closer to the center of the Brillouin zone.

As already mentioned, the identification of the mapping mechanism of the low-frequency vibrational mode in the high-energy reflectivity could be of fundamental importance in the interpretation of the statistical data obtained in the “monochromatic” pump-probe measurements reported in the previous section.

Figure 8.8: 0.5 mJ/cm^2 fluence

Figure 8.9: 2.5 mJ/cm^2 fluence

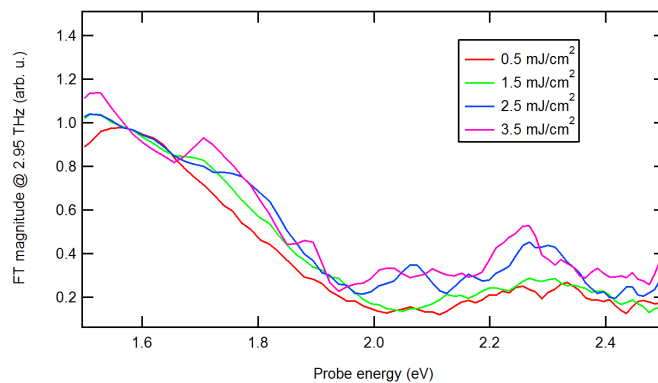


Figure 8.10: Normalized amplitude of the coherent contribution as a function of the probe energy.

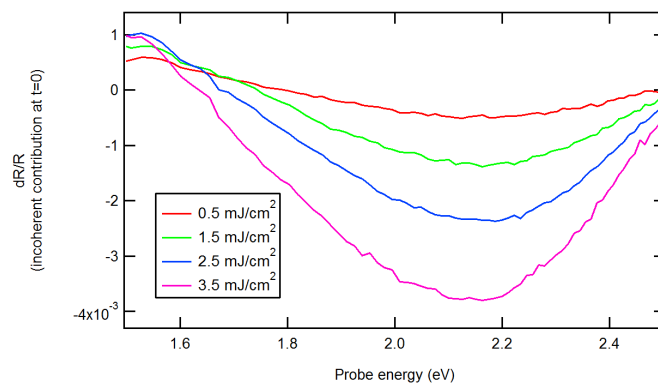


Figure 8.11: Incoherent contribution at 0 pump probe delay as a function of the probe energy.

8.3 Transient phase-shift

We report here an example of the measurements performed with the transient phase-shift set-up, described in chapter 6. The goal in building this set-up is to measure the transient phase variations $\Delta\theta(\omega)$ of the *field*-reflectivity

$$r(\omega) = |r(\omega)|e^{i\theta(\omega)}.$$

However, a more efficient procedure to extract the relevant information still has to be developed. Furthermore, the refinement of the set-up should be done using a sample which is known, from Kramers-Kronig calculations, to have large transient phase-shifts. This would provide a better starting point for the optimal calibration of the apparatus.

Nonetheless, from figures 8.12 and 8.13 of a measurement performed on Bismuth is clear that a small phase shift can be resolved, be it of thermal nature (due to pump-induced heating of the sample) or of electronic one. As described in chapter 6, the procedure to extract the phase-shift is to fit the red (at equilibrium) and blue (out of equilibrium) segments of the interferometric pattern with two different sinusoidal functions. In figure 8.13 we show that there is a phase difference between the equilibrium data and the out of equilibrium one. However, in order to perform a quantitative analysis, the experimental and analysis procedures should be refined.

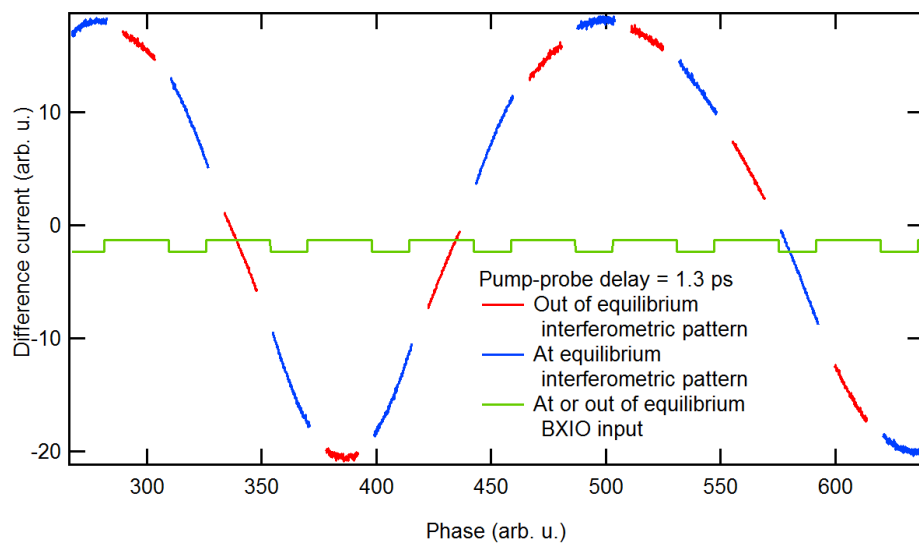


Figure 8.12: Example of interferometric pattern split in at and out of equilibrium sample.

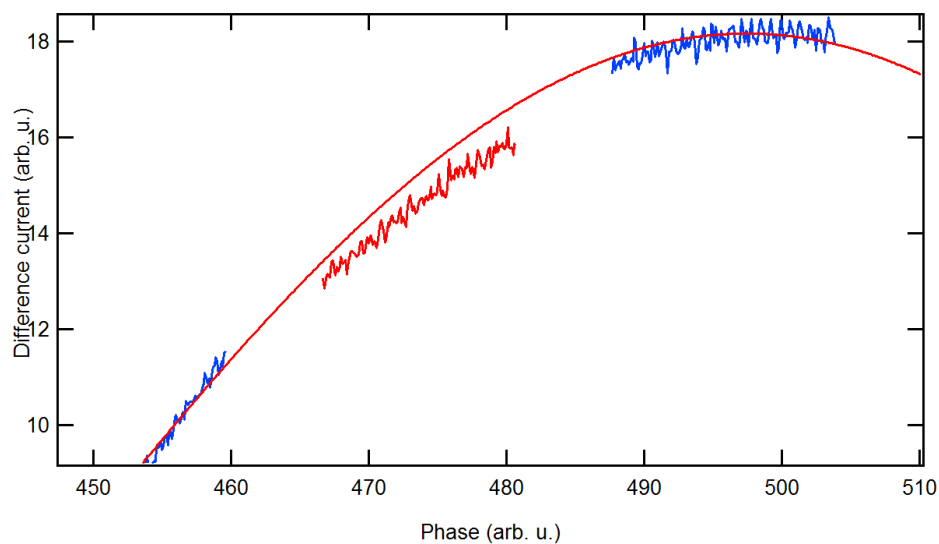


Figure 8.13: Zoomed view of a portion of the above graph.

Chapter 9

Discussion

The “monochromatic” reflectivity-noise data we have reported in the previous chapter offer many directions for their interpretation. While they allowed us to identify these various details to be studied, more systematic measurements must be performed in order to address the specific questions which have arisen. For these experiments, the laser stability should be optimized to avoid spurious contributions to the variance of the reflectivity signal. Denser fluence scans would be helpful for the clear identification of some trends. Moreover, lowering the repetition rate of the laser source would allow the exploration of higher excitation-fluence regimes.

However, some speculations are still possible starting from the set of available data. In particular, the most simple interpretations can be done for short pump-probe delays. In that limit, we consider only the effects of the excitation of the mode via the displacive excitation mechanism, and not the interactions of the vibrational mode with other degrees of freedom. The evolution of the reflectivity tells that these interactions play a major role in the phonon dynamics. As an example, with low excitation fluences the damping of the oscillation can be ascribed to the creation of phonons into modes of acoustical branches [31].

9.1 Possible squeezing of the lattice vibrations

There is a feature (shown in figure 9.1) in the first cycle of the variance’s oscillation, which appears only at high excitation-fluences and seems to be, therefore, a non-linear effect. In particular, it is a shoulder in the variance signal placed between the first maximum and the first minimum of the oscillation. There is also a mismatch between the minimum of the variance signal

and the one of the reflectivity. Figures 9.1a and 9.1b show a zoomed view of the first cycles of two high fluence measurements, the ones with damping time $\tau = 1.21$ ps and $\tau = 1.96$ ps.

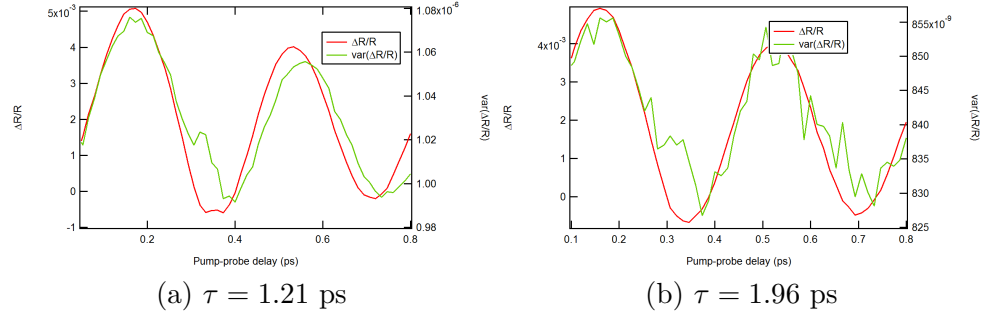


Figure 9.1: First cycles of the oscillations of the reflectivity and of its variance.

As a comparison, we report in figure 9.2 also a plot of the case in which the damping time τ is 2.82 ps, i.e. a low fluence one.

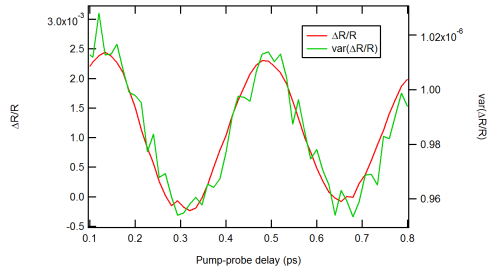


Figure 9.2: First cycles of the oscillations of the reflectivity and of its variance ($\tau = 2.82$ ps).

The coordinate of the vibrational mode is mapped in the reflectivity. As briefly discussed in chapter 3, as a function of the phase of the oscillation, the variance of \hat{q} of a mode in a squeezed state is modulated at twice the frequency of the mode itself.

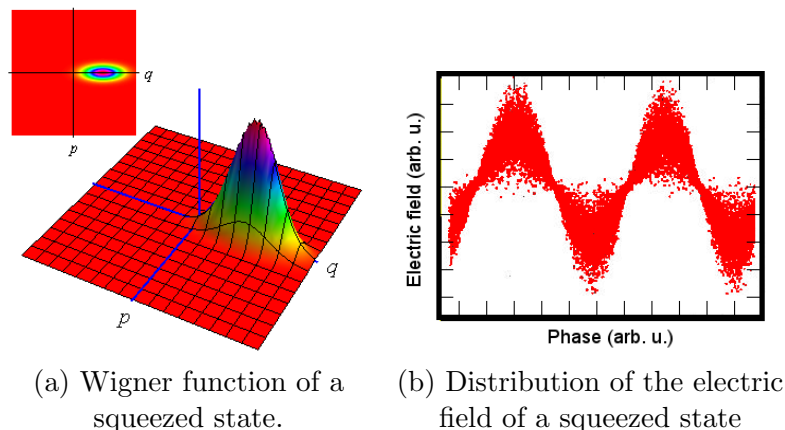


Figure 9.3: Squeezed state

In this context, the phase of the oscillation depends on the pump-probe delay. Since the time-resolution of pump-probe experiments is shorter than the period of the phonon oscillation, such a technique is phase-resolved for what concerns vibrational oscillations.

We must, however, consider that the variance we observe is the variance in the intensity of the probe, which contains contributions which come from different independent players. In particular, there are contributions which are intrinsic to the dynamics in the solid and contributions which are extrinsic to them.

In the following we will consider that the modulation of the reflectivity leads to a modulation of the probe's intensity. We expect, hence, a modulation of the shot-noise which follows exactly the reflectivity signal. Furthermore, there is a contribution to the variance which comes from the noise in the reflectivity of the sample itself. If the coordinate of a squeezed vibrational state were mapped into the reflectivity, the variance we measure would contain a term oscillating at twice the frequency of the reflectivity's oscillation. Considering just these two contributions (apart from the constant background), the variance would have a pump-probe delay-dependence given by the sum of a $\sin(t)$ term and a $\sin(2t)$ term.¹ (Note that we concentrate just on the first cycle, in order to neglect the frequency variations in time.) In figure 9.4 we plot the function

$$\sin(t) + a_0 \sin(2t)$$

¹We neglect here the fact that the initial frequency of the variance, as given by our fits, is different from the initial frequency of the reflectivity. In fact, their difference is very small and, at this stage, the argument we present is only qualitative.

for two different values of a_0 . $\sin(t)$ is plotted as a reference in both graphs.

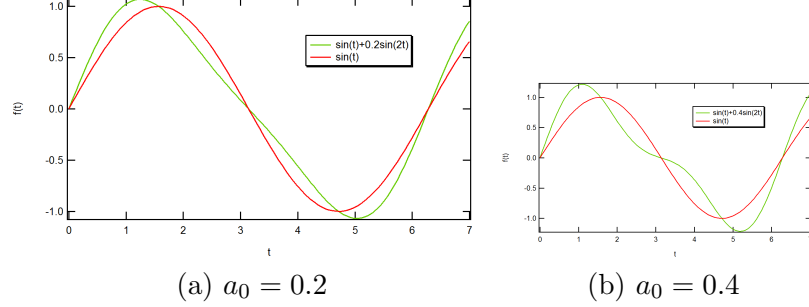


Figure 9.4: $\sin(t) + a_0 \sin(2t)$ for different values of a_0 .

By tuning a_0 , a feature similar to the shoulder and the mismatch present in the variance trace can be reproduced.

Since this behaviour takes place only at high excitation-fluence, the following hypothesis can be made. At low pump-fluences the vibrational mode is excited with the linear simple *displacive excitation* mechanism described in the context of the Jones-Peierls distortion for small potential-displacements. Such an interaction is linear in the phononic mode operators, since it consists in a change of the equilibrium position of the oscillator. In fact, the Hamiltonian in the harmonic approximation of the potential in which the atoms lie, is

$$\begin{aligned} \hat{H} &= \frac{\hat{p}^2}{2} + \frac{(\hat{q} - q_0)^2}{2} \\ &= \frac{\hat{p}^2}{2} + \frac{\hat{q}^2}{2} + \frac{q_0^2}{2} - q_0 \hat{q} \end{aligned} \quad (9.1)$$

The term representing the interaction of the electrons with the phononic mode is

$$- q_0 \hat{q}. \quad (9.2)$$

Expanding q_0 in the electron excitation density parameter n [21], it becomes²

$$- c_1 n \hat{q}. \quad (9.3)$$

This term can be written effectively as

$$\hat{H}_1 = \gamma_1 (\hat{a} \hat{b}^\dagger + \hat{a}^\dagger \hat{b}), \quad (9.4)$$

²Note that we are not considering the decay of $n(t)$ after the excitation in the short times limit in order to have a simple time dependence of the Hamiltonian.

where, as mentioned in chapter 4, \hat{a} and \hat{a}^\dagger refer to photonic modes and \hat{b} and \hat{b}^\dagger refer to phononic modes. Such a linear coupling must be mediated by the electrons (as it is in the Jones-Peierls mechanism [21]), since the A_{1g} mode is not electric dipole-active. In \hat{H}_1 the electronic degrees of freedom have been integrated out in the coupling constant γ_1 and the interaction is written as an effective photon-phonon coupling. Supposing a spatially homogeneous excitation of the electrons, the vibrational mode involved is at the centre of the Brillouin zone:

$$\hat{H}_1 = \gamma_1 (\hat{a} \hat{b}_0^\dagger + \hat{a}^\dagger \hat{b}_0), \quad (9.5)$$

where \hat{b}_0 is the annihilation operator of the $k = 0$ mode. As described in chapter 4, for what concerns the vibrational mode, such an Hamiltonian produces a displacement of the Wigner function of the mode. Therefore, in this fluence-regime, the excited vibrational state is a displaced thermal state. This means that the phonon-contribution to the variance is not phase-dependent.

Going to higher pump-fluences, and hence to larger potential displacements, other terms in the coupling become relevant. The next term in the Hamiltonian for the vibrational mode can be seen to be of second-order in the mode operators taking into account the known phonon softening due to “electronic screening” [28]:

$$\begin{aligned} \hat{H} &= \frac{\hat{p}^2}{2} + (1 + c_2 n) \frac{(\hat{q} - c_1 n)^2}{2} \\ &= \frac{\hat{p}^2}{2} + (1 + c_2 n) \left(\frac{\hat{q}^2}{2} + \frac{(c_1 n)^2}{2} - c_1 n \hat{q} \right) \\ &= \frac{\hat{p}^2}{2} + \frac{\hat{q}^2}{2} + (1 + c_2 n) \frac{(c_1 n)^2}{2} - (1 + c_2 n) c_1 n \hat{q} + \frac{c_2 n}{2} \hat{q}^2 \end{aligned} \quad (9.6)$$

The second-order term in the interaction Hamiltonian can be written as

$$\hat{H}_2 = \gamma_2 ((\hat{b}_0^\dagger)^2 + (\hat{b}_0)^2). \quad (9.7)$$

As shown in chapter 4, this Hamiltonian produces squeezed states, which have variances that oscillate as a function of the phase at twice the mode’s frequency.

The total first- and second-order interaction Hamiltonian is then

$$\hat{H}_{1,2} = \gamma'_1 (\hat{b}_0^\dagger + \hat{b}_0) + \gamma_2 ((\hat{b}_0^\dagger)^2 + (\hat{b}_0)^2), \quad (9.8)$$

where we have substituted \hat{a} with z because of the high fluence regime, and have absorbed it in γ'_1 . As already mentioned, the first-order term in this Hamiltonian could be what is generally described as *displacive excitation*,

while the second-order one becomes relevant in the high fluence-regime and hence large displacements of the atomic potential.

The most simple initial condition is that all the vibrational modes are at thermal equilibrium with the sample, i.e. their initial state is a thermal one. In the high-fluence regime, the density matrix of the final state produced (under these hypotheses) in the excitation is, at $t = 0^+$

$$\hat{\rho}(t = 0^+) = \hat{U}_t^\dagger \hat{\rho}_T \hat{U}_t. \quad (9.9)$$

It has been shown [5] that the linear and bilinear/quadratic term in $\hat{H}_{1,2}$ and in \hat{U}_t can be factorized to give a squeezing and a displacement operator. The final state can then be written as

$$\hat{\rho}(t = 0^+) = \hat{D}^\dagger(\alpha) \hat{S}^\dagger(\xi) \hat{\rho}_T(0) \hat{S}_2(\xi) \hat{D}(\alpha). \quad (9.10)$$

The initial and $t = 0^+$ Wigner functions for the mode at $k = 0$ are depicted in figure 9.5.

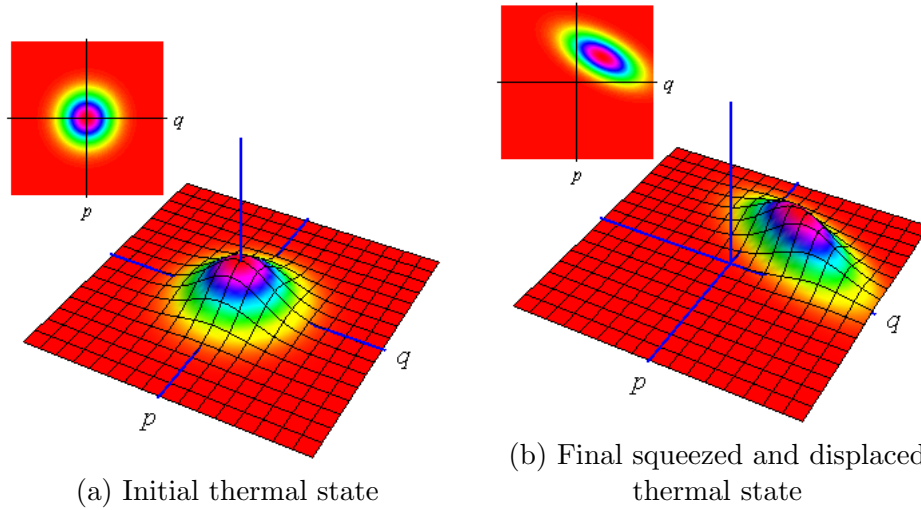


Figure 9.5: The initial and final Wigner function under these excitation hypotheses.

Chapter 10

Conclusions and perspectives

In this thesis we have shown that the framework developed in quantum optics to describe and study the modes of the electromagnetic field can be extended to condensed matter. It can be used to describe phenomena modelled with harmonic oscillators, such as vibrational dynamics in atomic lattices. We have analysed, from this point of view, the well known “coherent” vibrational response of Bismuth in pump-probe experiments. As we discussed, something that is classically “coherent” can correspond to different quantum states, and namely to coherent, squeezed and displaced thermal ones. The state of the vibrational mode is linked to the kinds of interactions it has undergone and, therefore, knowing it, one can deduce some of the characteristics of the Hamiltonians that determined its evolution.

We have presented two experimental set-ups we have built to study the state of systems in condensed matter. The first one, our pump-probe balanced homodyne detector, is a balanced homodyne detector adapted to study the state of the probe pulses after their interaction (i.e. reflection) with the excited sample in pump-probe experiments. The main question we will address is whether the sample dynamics can be mapped, not only into the intensity, but also in the state of the reflected pulse. This set-up still has to be refined before it can be used for such measurements.

The scheme for noise pump-probe measurements, instead, showed that it can be used to perform a partial characterization of the states which are mapped in the reflectivity of the sample. With such an apparatus we studied the statistical properties of the transient reflectivity of Bismuth. Its time-domain reflectivity is modulated following the expectation value of the position \hat{q} of the A_{1g} vibrational mode. Measuring the distribution of the values of $\frac{\Delta R}{R}(t)$

at a given t gives, therefore, access to the statistics of the underlying vibrational state. The data we collected suggest that the vibrational state excited with high pump-fluences may be a *squeezed* state. However, this conclusion should be supported by more measurements.

We also performed pump-probe measurements on Bismuth using white light probes. These experiments allow to track the transient reflectivity variation over a broad range of frequencies, in order to be able to draw a more complete picture of the dynamics induced by the pump-pulses.

The set-ups we have built give, moreover, the possibility to perform measurements of the transient phase-shift of the *field*-reflectivity in pump-probe experiments. While this technique is equivalent to the standard polarization ellipsometry, which is performed also in non-equilibrium conditions, to our knowledge this kind of phase-resolved measurements are not performed.

Current work in our group is concentrating on exploring how the reflection of the probe's light from the sample could map the state of a system in the solid into the quantum state of the probe itself. A scattering described by a linear Hamiltonian may lead just to encode some of the information in the variance of the measured intensity. This can be measured using our noise pump-probe set-up. However, it may be worth to explore the possibility of studying the state of, for example, Raman scattered light from the sample or other un-conventional "reflectivities" in order to extract information on the underlying dynamics.

Appendix A

Time evolution of a coherent state

The expectation value of the position \hat{q} of a harmonic oscillator in a coherent state oscillates in time at the frequency of the mode. This can be shown in the following way.

Let us express \hat{q} as

$$\hat{q} = \frac{1}{\sqrt{2}}(\hat{a} + \hat{a}^\dagger).$$

The evolution of the operators \hat{a} and \hat{a}^\dagger in the Heisenberg picture is given by

$$\begin{aligned}\dot{\hat{a}} &= i[\hat{H}(t), \hat{a}] \\ &= i\omega [\hat{a}^\dagger \hat{a}, \hat{a}] \\ &= i\omega [\hat{a}^\dagger, \hat{a}]\hat{a} \\ &= -i\omega \hat{a}.\end{aligned}$$

Therefore,

$$\hat{a}(t) = e^{-i\omega t} \hat{a}$$

and similarly for \hat{a}^\dagger

$$\hat{a}^\dagger = e^{i\omega t} \hat{a}^\dagger.$$

The expectation value of $\hat{q}(t)$ on a coherent state becomes, therefore,

$$\begin{aligned}
 \langle \hat{q}(t) \rangle_{|\alpha\rangle} &= \langle \alpha | \hat{q}(t) | \alpha \rangle \\
 &= \frac{1}{\sqrt{2}} \langle \alpha | \hat{a}(t) + \hat{a}^\dagger(t) | \alpha \rangle \\
 &= \frac{1}{\sqrt{2}} (e^{-i\omega t} \langle \alpha | \hat{a} | \alpha \rangle + e^{i\omega t} \langle \alpha | \hat{a}^\dagger | \alpha \rangle) \\
 &= \frac{1}{\sqrt{2}} (e^{-i\omega t} \alpha + e^{i\omega t} \alpha^*) \\
 &= \frac{1}{\sqrt{2}} 2 \mathcal{R}e(e^{-i\omega t} \alpha).
 \end{aligned}$$

In the following figures we report a comparison of classical and quantum harmonic oscillators in coherent states for three different times.

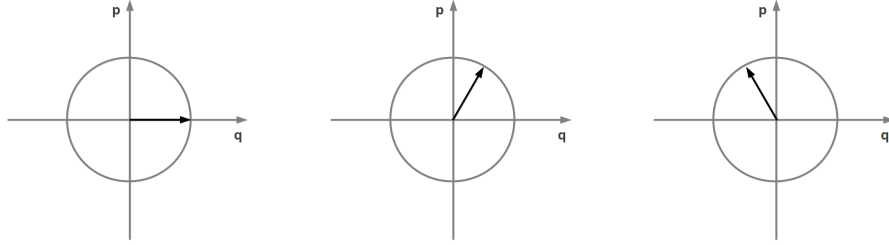


Figure A.1: Classical harmonic oscillator in a “coherent” state during its free time evolution.

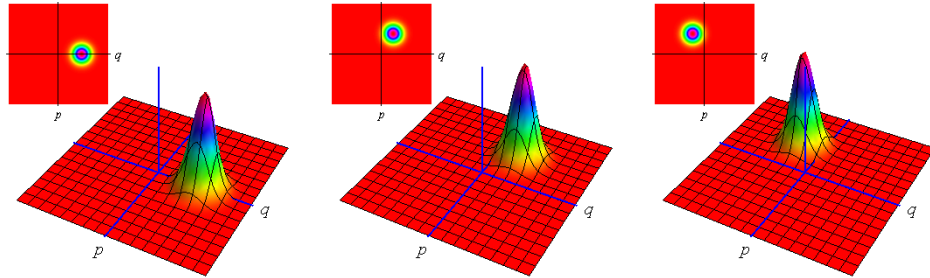


Figure A.2: Quantum harmonic oscillator in a coherent state during its free time evolution.

Appendix B

Quorum for a two-level system

In order to give a simple example of the need to measure a quorum of observables to reconstruct the density matrix, let's consider a two level-system. The Hilbert space \mathcal{H} of such a system is two-dimensional and the density matrix describing the state of the system can be written, in the $\{|0\rangle, |1\rangle\}$ base, as

$$\hat{\rho} = \begin{pmatrix} \rho_{00} & \rho_{01} \\ \rho_{10} & \rho_{11} \end{pmatrix}.$$

The diagonal elements, ρ_{00} and ρ_{11} are the probabilities of finding the system in the states $|0\rangle$ and $|1\rangle$, respectively. They can be measured as the normalized frequencies of observing the eigenvalues of $|0\rangle\langle 0|$ and $|1\rangle\langle 1|$. However, in order to fully reconstruct the density matrix, also the values of ρ_{01} and ρ_{10} must be measured. They are the mean values of the observables

$$\hat{O}_{01} = \frac{1}{\sqrt{2}}(|0\rangle\langle 1| + |1\rangle\langle 0|)$$
$$\hat{O}_{10} = \frac{1}{i\sqrt{2}}(|0\rangle\langle 1| - |1\rangle\langle 0|).$$

$|0\rangle\langle 0|$, $|1\rangle\langle 1|$, \hat{O}_{01} and \hat{O}_{10} constitute a quorum of observables. Their measurement allows the complete reconstruction of the density matrix ρ .

Appendix C

D_{3d} point group

The character table of the irreducible representations of the D_{3d} group is the following:

	E	$2C_3$	$3C_2$	i	$2S_6$	$3\sigma_d$	linear bases	quadratic bases
A_{1g}	1	1	1	1	1	1		$x^2 + y^2, z^2$
A_{2g}	1	1	-1	1	1	-1	R_z	
E_g	2	-1	0	2	-1	0	(R_x, R_y)	$(x^2 - y^2, xy)$ (xz, yz)
A_{1u}	1	1	1	-1	-1	-1		
A_{2u}	1	1	-1	-1	-1	1	z	
E_u	2	-1	0	-2	1	0	(x, y)	

Appendix D

Transient phase-shift and Kramers-Kronig relations

As an alternative to the direct measurement of the transient phase-shift, discussed in section 6.4, it is possible to estimate it starting from the knowledge of $\frac{\Delta R}{R}(t)$ over a broad range of energies and using the Kramers Kronig relations. This kind of data is the one acquired, for example, with the white-light pump-probe set-up described in section 6.3.

The complex *field*-reflectivity can be written as

$$r = |r(\omega)|e^{i\theta(\omega)},$$

where ω is the frequency of the electromagnetic wave. Using the Kramers-Kronig relations,

$$\theta(\omega_0) = \frac{\omega_0}{\pi} \mathcal{P} \int_0^\infty \frac{d\omega}{\omega_0^2 - \omega^2} \log(R(\omega)).$$

In the excited (or, pumped) situation,

$$\begin{aligned} \theta_p(\omega_0) &= \frac{\omega_0}{\pi} \mathcal{P} \int_0^\infty \frac{d\omega}{\omega_0^2 - \omega^2} \log(R_p(\omega)) \\ &= \frac{\omega_0}{\pi} \mathcal{P} \int_0^\infty \frac{d\omega}{\omega_0^2 - \omega^2} \log(R_{eq}(\omega) + \Delta R(\omega)) \\ &= \frac{\omega_0}{\pi} \mathcal{P} \int_0^\infty \frac{d\omega}{\omega_0^2 - \omega^2} \left\{ \log(R_{eq}(\omega)) + \log\left(1 + \frac{\Delta R(\omega)}{R_{eq}(\omega)}\right) \right\} \\ &= \theta_{eq}(\omega_0) + \Delta\theta(\omega_0), \end{aligned}$$

where p labels quantities in the pumped situation and eq instead the equilibrium ones. Therefore, to estimate $\Delta\theta(\omega_0, t)$ it is necessary to know $\frac{\Delta R}{R}(\omega_0, t)$

over a broad range of frequencies, while the knowledge of the equilibrium reflectivity is, in principle, unnecessary. If the integration is done on a finite frequency range, it is important for ω_0 to lie far from its borders, since the finite range-approximation would otherwise be unjustified.

Appendix E

Acquisition software

We have written the software for our experimental set-up in LabVIEW. It controls the piezo-translator, which is used to change the phase of the local oscillator in the interferometer, the micrometric stage, used to change the pump-probe delay, and the acquisition board with its options (Multiple Recording, BXIO).

The communication with the translators occurs over serial channels and the connections are managed using the VISA LabVIEW library. The commands are sent to the devices directly via the VISA library and, partially, using the LabVIEW drivers provided by the manufacturer (PI).

The acquisition board, instead, is directly mounted in a PCI-express slot of the PC. In this case, it is entirely managed using the provided drivers. Their initialization parameters allow to set the number of channels of the ADC to be acquired (1 or 2) and the Multiple Recording and BXIO options.

The main parameters for the Multiple Recording option are the numbers of samples to acquire *before* and *after* each trigger. These have to be set in order to acquire the data related to the entire response of the photodiode to a pulse. The data are downloaded from the acquisition board to the PC via the FIFO interface.

When the BXIO option is active, the status of the 8 digital BXIO channels are sent to the PC in the last 8 bits of the *timestamp*. The latter is a set of bytes sent together each sample acquired by the ADC.

Riassunto

La cinematica dei fenomeni coerenti nella materia condensata è generalmente descritta in modo classico. Un chiaro esempio a riguardo è il caso delle vibrazioni nei reticoli atomici. Infatti, mentre le loro interazioni con gli altri gradi di libertà del materiale vengono generalmente descritte come processi quantistici, lo stato del modo vibrazionale in sé è descritto da parametri classici: ampiezza e fase (oltre che dalla sua frequenza e momento). Tranne che in casi limitati, le proprietà statistiche degli stati nella materia condensata, introdotte quando si descrive il sistema come un oggetto quantistico, non vengono considerate, nonostante questo tipo di informazioni possa porre dei vincoli su quale sia la dinamica a cui è soggetto il sistema. La conoscenza dello stato quantistico di un sistema durante la sua evoluzione può, per alcuni aspetti, determinare l'Hamiltoniano che la descrive.

Durante il lavoro per questa tesi abbiamo studiato gli stati vibrazionali nei solidi e, in particolare, abbiamo scelto un cristallo di Bismuto come sistema modello poiché mostra una risposta vibrazionale coerente negli esperimenti di pump-probe. In un esperimento di pump-probe il campione è portato fuori equilibrio tramite un impulso di luce ultracorto molto intenso (detto pompa) e la sua risposta ottica transiente (come ad esempio la variazione della sua riflettività) viene studiata grazie ad un secondo impulso di luce ultracorto, meno intenso del primo (detto *probe*, o sonda). Modificando il ritardo tra l'eccitazione e la misura (detto pump-probe *delay*) si può studiare come le proprietà ottiche del materiale evolvono nel tempo. Nel caso del Bismuto, l'impulso di pompa eccita un modo fononico a simmetria A_{1g} e l'oscillazione coerente della coordinata di quest'ultimo viene osservata nella misura della riflettività ad alta energia del campione.

La risposta coerente nel Bismuto è spiegabile nel contesto del meccanismo di Jones-Peierls [20, 19]: la struttura del cristallo elementare di Bismuto è descrivibile come una struttura cubica semplice distorta, in cui è avvenuta una dimerizzazione lungo la direzione [111]. Il cristallo risulta quindi essere

cubico a facce centrate, con due atomi per cella. Poiché la distorsione e la conseguente riduzione di simmetria sono favorite da un guadagno netto in energia elettronica tramite il meccanismo di Jones-Peierls, la riduzione di guadagno energetico provocata dall'eccitazione elettronica da parte della pompa destabilizza la struttura distorta, inducendo delle vibrazioni coerenti lungo la direzione [111] del cristallo. Questo tipo di eccitazione viene chiamato *displacive excitation*. La direzione [111] è quella propria del modo vibrazionale A_{1g} , che, a seguito dell'eccitazione con la pompa, presenta quindi un valore della sua coordinata che oscilla coerentemente nel tempo. Tuttavia, oscillazioni coerenti della coordinata \hat{q} e del momento \hat{p} di un oscillatore armonico corrispondono a più stati quantistici diversi, come ad esempio gli stati coerenti e gli stati *squeezed*. Ciò che li distingue sono le proprietà statistiche della misura delle loro osservabili.

Il *framework* dell'ottica quantistica offre degli strumenti molto potenti per trattare la varietà di stati dell'oscillatore armonico quantistico. Essa infatti riguarda la trattazione quantistica dei modi del campo elettromagnetico, che sono descritti da oscillatori armonici come i modi vibrazionali nei solidi. Inoltre, negli ultimi vent'anni è stata sviluppata e perfezionata una tecnica, chiamata rivelazione omodina bilanciata (*balanced homodyne detection*), che permette di studiare gli stati quantistici dei modi della radiazione elettromagnetica. La rivelazione omodina è un'implementazione del processo detto tomografia quantistica, nel quale viene ricostruita la matrice densità dello stato del sistema studiato. Ciò è possibile attraverso la misura ripetuta (su copie identiche del sistema) di un insieme di osservabili del sistema detto *quorum di osservabili*.

Le misure omodine bilanciate consistono in misure interferometriche (e quindi, risolte in fase) della distribuzione dei valori del campo elettrico del modo che si vuole studiare. Quest'ultimo viene mescolato su un *beam-splitter* 50-50 con un modo in uno stato coerente popolato da un alto numero di fotoni. La differenza tra le intensità dei due fasci uscenti dal *beam-splitter* vengono misurate grazie ad un detector bilanciato, in cui viene amplificata la differenza tra le fotocorrenti prodotte in due fotodiodi.

Queste misure vengono effettuate comunemente nei laboratori di ottica quantistica per caratterizzare lo stato di un modo della radiazione dopo le interazioni con i sistemi fisici posti sul suo cammino ottico (*beam-splitter*, dispositivi ottici non lineari, ecc.).

Dati questi strumenti è naturale chiedersi se, nell'interazione degli impulsi di *probe* con il campione fuori equilibrio (ovvero nella loro riflessione), informazioni sullo stato del campione possano venir mappate nello stato ottico del

probe. Qualora questo fosse possibile tale informazione può essere poi estratta effettuando la tomografia dello stato dell'impulso di luce. Abbiamo sviluppato, pertanto, un apparato sperimentale che combina la tecnica omodina bilanciata con quella di pump-probe. Esso dovrà però essere perfezionato nei prossimi mesi e ne presentiamo soltanto la caratterizzazione.

Esistono, tuttavia, altre tecniche che permettono di accedere ad informazioni statistiche, sebbene parziali, sugli stati nella materia condensata. In particolare, abbiamo sviluppato un apparato che permette di misurare non solo la variazione di riflettività negli esperimenti di pump-probe, ma anche la sua varianza per ciascun pump-probe *delay*. Le nostre misure hanno dimostrato che effettuando misure di questo tipo su sistemi in cui si osserva una risposta vibrazionale coerente, come il Bismuto, è possibile ottenere informazioni statistiche sullo stato del modo fononico coinvolto. Queste misure sono, per alcuni aspetti, simili ad una misura omodina, poiché la misura della coordinata del modo fononico è risolta in fase, ma esistono fattori, come le interazioni del modo con altri gradi di libertà, che le rendono non completamente tomografiche.

L'apparato che abbiamo costruito per effettuare queste misure si basa sullo stesso detector bilanciato utilizzato per le misure omodine ed in particolare i due apparati sono compatibili, ovvero è possibile passare da uno all'altro semplicemente sollevando due specchi posti su dei montaggi ribaltabili. Su uno dei due fotodiodi del detector incide un fascio impulsato di riferimento, mentre sul secondo viene focalizzato il fascio di probe. In questo modo, quando

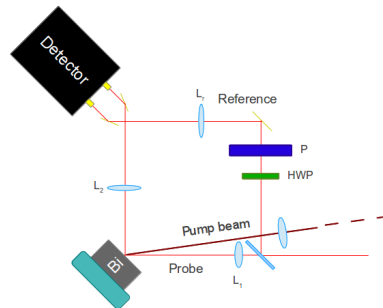


Figure 1: Schema semplificato dell'apparato bilanciato per le misure di pump-probe.

l'intensità del fascio di probe cambia a seguito della variazione della riflettività ΔR del campione, il segnale differenziale in uscita dal detector è direttamente

proporzionale a ΔR . Grazie ad un digitalizzatore veloce possiamo acquisire un valore di ΔR per ciascun impulso di probe. Pertanto, i tempi di acquisizione di grandi quantità di dati sono molto piccoli, in quanto ogni secondo è possibile acquisire tante volte il valore di ΔR quanti sono gli impulsi prodotti dal laser, ovvero 250 000. Le medie di questi numeri calcolate per ogni pump-probe *delay* costituiscono la consueta traccia di pump-probe, che mostra la variazione di riflettività del campione in funzione del tempo. Ma per ciascun pump-probe *delay* è possibile calcolare anche la varianza dei valori di ΔR misurati.

Come già anticipato e come già noto, la variazione della riflettività del campione di Bismuto è modulata alla frequenza del modo A_{1g} , che viene ammorbitata per tempi brevi quando la densità di eccitazioni elettroniche è alta. Ciò che abbiamo osservato è che anche la varianza è modulata coerentemente. Per basse densità di eccitazioni le frequenze delle modulazioni di $\Delta R(t)$ e della sua varianza sono molto simili o coincidono. Ciò è giustificabile considerando che, a variazioni di intensità degli impulsi di *probe* riflessi corrispondono variazioni nello *shot noise* dello stato ottico stesso. Per alte densità di eccitazioni, invece, la frequenze delle due differiscono significativamente.

Inoltre, il primo ciclo dell'oscillazione della varianza mostra una spalla. Essa è riproducibile se si considera, oltre al contributo dello *shot noise* alla varianza, che oscilla come $\sin(\omega t)$, un termine del tipo $\sin(2\omega t)$, proprio della varianza della coordinata di un oscillatore armonico preparato in uno stato *squeezed*. Per basse densità di eccitazioni, il meccanismo della *displacive excitation* è descritto da un Hamiltoniano lineare negli operatori del modo fononico (ovvero, \hat{b} e \hat{b}^\dagger) e produce stati coerenti, in cui la varianza della posizione \hat{q} non dipende dalla fase dell'oscillazione. Per alte densità, invece, termini quadratici dell'Hamiltoniano di interazione diventano rilevanti e, un'interazione del tipo

$$H = \lambda \hat{b}^\dagger + \zeta (\hat{b}^\dagger)^2 + \text{h. c.}$$

porta l'oscillatore armonico in uno stato *squeezed*.

Tuttavia, dovrebbero essere effettuate altre misure a supporto di questa ipotesi.

Oltre a queste misure abbiamo effettuato anche esperimenti di pump-probe sullo stesso campione con *probe* di luce bianca. Essi permettono di studiare la risposta ottica del materiale su un ampio intervallo di lunghezze d'onda, in modo da avere un'immagine più chiara delle dinamiche indotte dall'eccitazione.

Inoltre, l'interferometro dell'apparato per le misure omodine può essere utilizzato, sempre nell'ambito degli esperimenti di pump-probe, per misurare le

variazioni transienti della fase del campo elettrico del *probe* riflesso dal campione. Di questo schema abbiamo presentato una caratterizzazione e una misura preliminare.

Bibliography

- [1] Ugo Fano. Description of states in quantum mechanics by density matrix and operator techniques. *Reviews of Modern Physics*, 29(1):74–93, 1957.
- [2] Huedong Xu and Franco Nori. Phonon squeezed states: quantum noise reduction in solids. *Physica B*, 263-264:16–29, 1999.
- [3] Neil W. Ashcroft and N. David Mermin. *Solid State Physics*. BROOKS/COLE CENGAGE Learning, 1976.
- [4] Alessandro Ferraro, Stefano Olivares, and Matteo Paris. Gaussian states in continuous variable quantum information. *ArXiv*, 2004.
- [5] Xu Huedong. *Quantum fluctuations in condensed matter systems: squeezed states in phonons and Josephson junctions*. PhD thesis, University of Michigan, 1996.
- [6] D. T. Smithley, M. Beck, and M. G. Raymer. Measurement of the Wigner distribution and the density matrix of a light mode using optical homodyne tomography: Application to squeezed states and the vacuum. *Physical Review Letters*, 70(9):1244–1247, 1993.
- [7] K. Vogel and H. Risken. Determination of quasiprobability distributions in terms of probability distributions for the rotated quadrature phase. *Physical Review A*, 40(5):2847–2849, 1989.
- [8] G. M. D’Ariano, C. Macchiavello, and M. G. A. Paris. Detection of the density matrix through optical homodyne tomography without filtered back projection. *Physical Review A*, 50:4298–4302, 1994.
- [9] G. M. D’Ariano, U. Leonhardt, and H. Paul. Homodyne detection of the density matrix of the radiation field. *Physical Review A*, 52(3):1801–1804, 1995.

- [10] G. Mauro D'Ariano, Matteo G. A. Paris, and Massimiliano F. Sacchi. Quantum tomography. *Advances in Imaging and Electron Physics*, 128:205–308, 2003.
- [11] Mark Fox. *Quantum Optics, An Introduction*. Oxford University Press, 2006.
- [12] A. I. Lvovsky and M. G. Raymer. Continuous-variable optical quantum-state tomography. *Reviews of Modern Physics*, 81(1):299–332, 2009.
- [13] Juergen Appel, Dallas Hoffmann, Eden Figueroa, and A. I. Lvovsky. Electronic Noise in Optical Homodyne Tomography. *Physical Review A*, 75:035802, 2007.
- [14] J. M. Aubry, C. Butucea, and K. Meziani. State estimation in quantum homodyne tomography with noisy data. *Inverse Problems*, 25(1):015003, 2008.
- [15] Leonid A. Krivitsky, Ulrik L. Andersen, Ruifang Dong, Alexander Huck, Christoffer Wittmann, and Gerd Leuchs. Correlation measurement of squeezed light. *Physical Review A*, 79:033828, 2009.
- [16] Oleg V. Misochko. Coherent Phonons and Their Properties. *Journal of Experimental and Theoretical Physics*, 92(2):246–259, 2001.
- [17] A. Hussain and S. R. Andrews. Absence of phase-dependent noise in time-domain reflectivity studies of impulsively excited phonons. *Physical Review B*, 81:224304, 2010.
- [18] Daniele Fausti. *Phase Transitions and Optically Induced Phenomena in Cooperative Systems*. PhD thesis, Rijksuniversiteit Groningen, 2008.
- [19] Rudolf Ernst Peierls. *More surprises in theoretical physics*. Princeton University Press, 1991.
- [20] Harry Jones. Applications of the Bloch Theory to the Study of Alloys and of the Properties of Bismuth. In *Proc. Roy. Soc. A147:396*, 1934.
- [21] H. J. Zeiger, J. Vidal, T. K. Cheng, E. P. Ippen, G. Dresselhaus, and M. S. Dresselhaus. Theory for dispersive excitation of coherent phonons. *Physical Review B*, 45(2):768–778, 1992.
- [22] M. Hase, K. Mizoguchi, H. Harima, S. Nakashima, M. Tani, K. Sakai, and M. Hangyo. Optical control of coherent optical phonons in Bismuth films. *Applied Physics Letters*, 69(17):2474–2476, 1996.

- [23] K. Ishioka, M. Kitajima, and O.V. Misochko. Temperature dependence of coherent A_{1g} and E_g phonons in Bismuth. *J. of Applied Physics*, 100:093501, 2006.
- [24] M. Hase, M. Kitajima, S. Nakashima, and K. Mizoguchi. Dynamics of Coherent Anharmonic Phonons in Bismuth Using High Density Photoexcitation. *Physical Review Letters*, 88:067401, 2002.
- [25] M. F. DeCamp, D. A. Reis, P.H. Bucksbaum, and R. Merlin. Dynamics and coherent control of high-amplitude optical phonons in Bismuth. *Physical Review B*, 64:092301, 2001.
- [26] O.V. Misochko, K. Ishioka, M. Hase, and M. Kitajima. Fano interference for large amplitude coherent phonons in Bismuth. *J. Phys. Condensed Matter*, 19(15):156227, 2007.
- [27] S. Fahy and D. A. Reis. Coherent Phonons: Electronic Softening or Anharmonicity? *Physical Review Letters*, 93:109701, 2004.
- [28] Daniele Fausti, Oleg Misochko, and Paul Van Loosdrecht. Ultrafast photoinduced structure phase transition in antimony single crystals. *Physical Review B*, 80:161207, 2009.
- [29] Francesco Randi. Generazione e caratterizzazione di un impulso supercontinuo di luce bianca. <https://sites.google.com/site/danielefausti/educational-materials>.
- [30] E. Papalazarou, J. Faure, J. Mauchain, M. Marsi, A. Taleb-Ibrahimi, I. Reshetnyak, A. van Roekeghem, I. Timrov, N. Vast, B. Arnaud, and L. Perfetti. Coherent Phonon Coupling to Individual Bloch States in Photoexcited Bismuth. *Physical Review Letters*, 108:256808, 2012.
- [31] M. Hase, M. Kitajima, S. Nakashima, and K. Mizoguchi. Dynamics of coherent phonons in Bismuth generated by ultrashort laser pulses. *Physical Review B*, 58(9):5448–5452, 1998.

Ringraziamenti

Il mio primo ringraziamento va a Martina, per le discussioni fruttuose, per avermi insegnato tutto ciò che c'era da sapere sull'omodina, per il suo punto di vista sempre prezioso, le giornate in laboratorio... e anche per gli allineamenti degli specchi. E perché è grazie al suo lavoro di tesi che è nato il gruppo di ricerca allargato con cui ho avuto l'opportunità di lavorare in questi ultimi otto mesi. Daniele è riuscito a guidarmi verso un progetto che, ogni sera, non mi faceva vedere l'ora di andare in laboratorio la mattina successiva. Lo ringrazio per il suo entusiasmo e per tutto il tempo che ha dedicato e dedica a trasmettermelo e a spiegarmi cose nuove. Il suo ruolo è tra i più importanti in questi anni. Fulvio Parmigiani, per la sua presenza costante in questo progetto. Perché è sempre in grado di ampliare le vedute altrui e si assicura che ci sia sempre legna da ardere.

Grazie a Fabio Benatti, Roberto Floreanini e Stefano Olivares per i confronti che hanno reso chiare molte delle idee che ruotano attorno a questo progetto e perché mi hanno dato degli strumenti che altrimenti non avrei avuto l'occasione di ottenere.

Grazie a Fabio, Federico, Marco, Kelvin, Alberto, Goran, Marta, Valentina, Michele, Martina del gruppo T-ReX di Fermi@Elettra e non, per gli stimoli, le idee e le discussioni di questi mesi (compresa quella sulla fotoemissione dicroica).

E poi fuori dal laboratorio, i miei amici per i cinque anni passati insieme. È anche grazie a loro che sto così bene in questa città. E infine la mia famiglia e tutti coloro che ho incontrato prima dell'università, Stefano e Maddalena in particolare, perché con loro sono cresciuto.